Astronomy & Astrophysics manuscript no. lp_CITPM
March 26, 2021

Properties of slowly rotating asteroids from Convex Inversion Thermophysical Model

A. Marciniak[1], J. Ďurech[2], V. Alí-Lagoa[3], W. Ogłoza[4], R. Szakáts[5], T. G. Müller[3], L. Molnár[5,6], A. Pál[5,7], R. Behrend[8], L. Bernasconi[9], J. Bosch[10], S. Brincat[11], L. Brunetto[12], M. Butkiewicz - Bąk[1], F. Del Freo[13], R. Duffard[14], G. Farroni[15], S. Fauvaud[16], M. Fauvaud[16], M. Ferrais[17], S. Geier[18,19], J. Golonka[20], J. Grice[21], R. Hirsch[1], J. Horbowicz[1], E. Jehin[22], P. Julien[13], Cs. Kalup[5], K. Kamiński[1], M. K. Kamińska[1], P. Kankiewicz[23], V. Kecskeméthy[5], D.-H. Kim[24,25], M.-J. Kim[25], I. Konstanciak[1], J. Krajewski[1], V. Kudak[26,27], P. Kulczak[1], T. Kundera[4], F. Manzini[12], F. Monteiro[28], N. Morales[14], J. Nadolny[29], D. Oszkiewicz[1], E. Pakštienė[30], M. Pawłowski[1], V. Perig[27], F. Pilcher[31], P. Pinel[†15], E. Podlewska-Gaca[1], T. Polakis[32], F. Richard[16], R. Roy[30], J. J. Sanabria[20], T. Santana-Ros[34,35], B. Skiff[36], J. Skrzypek[1], K. Sobkowiak[1], E. Sonbas[37], G. Stachowski[4], J. Strajnic[13], P. Trela[1], Ł. Tychoniec[38], S. Urakawa[39], E. Verebelyi[5], K. Wagrez[13], M. Żejmo[40], and K. Żukowski[1]

(Affiliations can be found after the references)

Received xx xx xx / Accepted xx xx xx

ABSTRACT

Context. Recent results for asteroid rotation periods from TESS mission showed how strongly has the number of slow rotators been underestimated by all previous studies, revealing the importance to study those targets. Slowly rotating asteroids (here: those with period longer than 12 hours) largely lack spin and shape models due to observing selection effects, that also hamper the possibility to determine their thermal parameters and accurate sizes, while it is still unclear whether signatures of different surface material properties can mainfest themselves in thermal inertia determined from mid-infrared thermal flux fitting.

Aims. We continue our campaign aimed at decreasing selection effects among main belt asteroids. Our targets are slow rotators with low lighturve amplitudes. The aim is to provide their scaled spin and shape models together with thermal inertia, albedo, and surface roughness to complete the statistics, and to further check if there is any correlation between the thermal inertia and rotation period.

Methods. Rich multi-apparition datasets of dense lightcurves resulting from our photometric campaign conducted at a worldwide network of small telescopes is supplemented with lightcurves from the literature and also data from TESS spacecraft. In addition to data in the visible range, we also use thermal data from infrared space observatories (mainly IRAS, AKARI and WISE) in a combined optimisation process using the Convex Inversion Thermophysical Model. That novel method has so far been demonstrated to work on only a few targets so the aim was also to validate the method itself.

Results. We present the models of 16 slow rotators, including two updated models, that provide good fits to both thermal and visible data. Obtained sizes are on average accurate at 5% precision level. The rotation periods of our targets range from 11 to 59 hours, and the thermal inertia reaches wide range of values, from 2 to <400 SI units, not showing any correlation with the period. The diameters of our targets range from 25 to 145 km.

Conclusions. With this work we further substantially increase the sample of slow rotators with reliable spin and shape model based on dense lightcurves, and the pool of asteroids with known thermal inertia, making them available for further studies. The thermal inertia values of our sample do not display previously suggested increasing trend with rotation period, which might be due to relatively small skin depth.

Key words. minor planets: asteroids – techniques: photometric – radiation mechanisms: thermal

1. Introduction

Physical parameters of asteroids like spin, shape, size, albedo, macroscopic roughness or thermal inertia are an important basis for solar system studies, as large asteroids are considered remnants of early planetary formation. Studying the way in which asteroid surfaces react to the heating by the Sun (which, among others, depends on the spin axis inclination and spin rate), can reveal material properties of these layers. Slowly rotating asteroids, with periods longer than 12 hours, are especially interesting in this respect, as they experience long periods of irradiation of the same surface parts, and the heat wave can penetrate to deeper layers. Also, the newest results from TESS mission revealed enormous number of slow rotators among main-belt asteroids, proving that slow rotators actually dominate in the population, while being largely omitted by most of ground-based studies (see fig. 7 in Pál et al. 2020) mainly due to telescope time limitations, and few targeted campaigns.

As a consequence, the statistics of available spin and shape modelled asteroids are strongly biased towards faster rotators, where physical processes, like e.g. YORP effect efficiency, are different (Vokrouhlický et al. 2015). This might have implications on e.g. known spatial spin axis distribution as the outcome of the YORP effect or on the estimated contribution of tumblers and binaries in various asteroid populations.

Another hidden problem is that most of the well studied asteroids, especially among slow rotators, are those with large amplitudes of their lightcurves - being elongated in shape and having high spin axis inclination. In our survey, described in detail in Marciniak et al. (2015), we address both biases at the same time, focusing on slow rotators (P>12 hours) with maximum amplitudes not larger than 0.25 mag, at least at the target selection stage. During our study, a few targets appeared to have somewhat

larger amplitudes or shorter periods, but nevertheless remained in our target list.

The statistics in the set of asteroids with reliably determined thermal inertia are even more biased: counting the targets in compilation of previously published and new values by Hanuš et al. (2018), and the results from our earlier works: Marciniak et al. (2018), Marciniak et al. (2019), there are currently 36 main belt slow rotators (P>12 h) against 120 fast rotators (P<12 h) studied using detailed thermophysical modelling (TPM). This shows that in terms of sudying slow rotators in the infrared we only touched the tip of an iceberg.

Thermal inertia depends on the density of surface regolith, thermal conductivity, and heat capacity. Larger thermal inertia implies coarser regolith, composed of grain sizes of the order of millimeters to centimeters, typical for young surfaces of small Near Earth Asteroids (Gundlach & Blum 2013), while much finer, lunar-like regolith, with grain sizes between 10 and 100 microns is expected at large (D>100 km) main-belt asteroids. This picture might however be complicated by various family formation ages, recent catastrophic evens refreshing the surface, or by the presence of surface cohesion forces (Rozitis et al. 2014). Also, in the light of recent results for in-situ studied targets Ryugu and Bennu (Okada et al. 2020; Walsh et al. 2019) this standard interpretation of thermal inertia vs. surface fails - there are boulders on the surface with relatively low thermal inertia, while one would expect regolith. Thermal conductivity, and thus thermal inertia dependance on temperature at various subsurface depths is another factor to be considered. It has been shown that sub-millimiter flux probes deeper layers, carrying information on the conditions in them (Keihm et al. 2012). Also, thermal fatigue as a result of thermal cracking might be more pronounced for slow rotators (Delbo et al. 2014), due to larger contrast between day and night-time temperatures, decreasing thermal inertia due to production of more regolith. However, slower rotation also results in smaller number of thermal cycles over long time scales, lessening the efficiency of thermal cracking, so the combined influence of the two factors might cancel out.

Initially inspired by a suggestion by Harris & Drube (2016) that asteroid thermal inertia estimated from beaming parameter from WISE spacecraft results seemed to increase with increasing rotation period, we added thermophysical analysis to our study of slow rotators. At first, our results seemed to confirm this hypothesis (Marciniak et al. 2018), as we found large and medium termal inertia values for the first sample of 5 targets. Later, with twice as large sample, we found rather wide range (Marciniak et al. 2019), from very small to medium, similarly as Hanuš et al. (2018), generally not showing any trend with the rotation period. Still, the sample of asteroids with known thermal inertia within this period range remains small, so here we continue our study, however using a different approach.

One of possible two miror spin and shape solutions, that are the usual outcome of lightcurve inversion applied to targets orbiting close to the ecliptic plane, can sometimes accidentally fit thermal data better than the other. However, this can stem from the high sensitivity of thermal flux to small-scale shape details, and might not in fact point truly better spin solution. Thus we decided to switch from independent lightcurve inversion followed by thermophysical modelling of a fixed shape, to simultaneous optimisation of both types of data. The method enabling this approach is Convex Inversion Thermophysical Model, introduced in Ďurech et al. (2017). It also enables weighting two types of data relative to each other, to avoid the dominance of one data type of a cost of the other type.

In the following section the visible and infrared data used for modelling are described, next section presents the main features of the method for combined optical and mid-infrared photometric inversion, which is followed by the description of resulting models, and scaling those models by multi-chord stellar occultations, where available. In the last section we summarise the results and present the ideas for future work.

2. Visible and infrared data

Data for traditional, dense lightcurves in the visible range have been gathered in the framework of our long-term photometric campaign conducted since the year 2013, and described in Marciniak et al. (2015), including target selection criteria. The project now engages over 20 observing stations worldwide, performing regular observations on telescopes up to 1-m in diameter of a few tens of slowly rotating, main-belt asteroids with small amplitudes of brightness variations. Data for some targets also came from TESS space observatory (Pál et al. 2020), now available at the web archive[1], but also from Kepler Space Telescope dedicated proposal in the extended K2 mission (Howell et al. 2014), and Super WASP sky survey (Grice & et al. 2017)[2]. From the latter archive we only used subsets of best quality, choosing from targets with Super WASP datapoints already folded in lightcurves. Choosing a subset from those vast datasets was neccessary due to their abundance, in order to avoid dominance of one apparition over others, where much less datapoints were gathered in our programme; but also due to their intrinsic noise, sometimes preventing the identification of unique model solution over the whole dataset. The selection criteria for best Super WASP lightcurve fragments were the least photometric scatter and possibly vast range of observing dates.

In our observing campaign separate relative lightcurve fragments obtained in R filter or unfiltered, are later combined together creating composite lightcurves (Figs. 45 - 110 in the Appendix) using the criterion of minimum scatter between datapoints, for initial period determinations. We present the lightcurves that covered most of the rotation period and showed clear brightness variations, still for modelling we used all the data described in Table 4. Determined synodic periods should be generally in agreement in all apparitions, with only small, up to a few promile differences due to changes in relative velocity of the observer and the source. Synodic period range from various apparitions, extended at least three times is a range on which the precise, sidereal period is later searched in the lightcurve inversion procedure.

Composite lightcurves from various apparitions depict the general character of the asteroid shape (if regular and symmetric, or quite the opposite) and their changes are due to phase angle effects caused by topographic features shadowing, and different viewing geometries (aspect angles). Apart from ensuring a full period coverage, of sometimes tens of hours long period, we paid special attention to obtain data at possibly widest range of both ecliptic longitudes and phase angles (see Table 4 in the Appendix), which is a neccessary prerequisite for shape reconstruction (Kaasalainen & Durech 2020). Lightcurves presented in the Appendix also prove good quality of the photometry, with scatter of the order of 0.01 mag down to a few millimagnitudes, clearly depicting bightness variations in detail, in spite of very small amplitudes in some cases.

[1] https://archive.konkoly.hu/pub/tssys/dr1/

[2] http://asteroids.neilparley.com/asteroids/lc.html

Relative photometric data, after serving for initial convex inversion spin and shape modelling, were subsequently supplemented with V-band calibrated sparse in time data from USNO archive, downloaded from AstDys site[3], neccessary for size and albedo determinations in the application of full Convex Inversion Thermophysical Model. We restricted only to USNO archive due to relatively best quality of this set among the readily available calibrated data for asteroids. As has been shown by Hanuš et al. (2011) the median accuracy of USNO data is at the level of 0.15 magnitude.

Thermal infrared data were downloaded from SBNAF Infrared Database[4] (Szakáts et al. 2020), which is a convenient source, providing expert-reduced data products from main infrared space missions (AKARI, IRAS, WISE, Herschel, MSX, and ISO) also providing all the neccessary auxiliary information, like the observing geometry, colour correction, or overall measurement uncertainties. This database stores calibrated flux densities obtained via careful consideration of instrument specific calibration and processing procedures. Also, it ensures that the infrared data are purely thermal, with a negligible contribution of the reflected solar radiation. All the measurement uncertainty values have been reanalysed for the sake of database consistency, and include contributions from in-band flux density uncertainty, absolute calibration errors, and colour correction uncertanties. The infrared data for our targets came mostly from three missions: WISE (Wright et al. 2010) at 11.1 μm and 22.64 μm, AKARI (Murakami et al. 2007) at 9 and 18 μm, and IRAS (Neugebauer et al. 1984) at 12, 25, 60 and 100 μm, occassionally supplemeted with data from MSX (Egan et al. 2003) at 8.28, 12.13, 14.65, and 21.34 μm, where available. Usually all the infrared datapoints were used, except for single cases where clear outliers were detected, unable to be fitted by any of the models. Also, due to large size of some tagets resulting in large infrared flux, sometimes a subset or all WISE data at 11μ m have been partially saturated, and could not be used in pour analysis.

3. Convex Inversion Thermophysical Model

To fit optical lightcurves and thermal infrared data, we used a combined inversion of both data types developed by Ďurech et al. (2017) called the Convex Inversion Thermophysical Model (CITPM). The method combines convex inversion of lighcurves (Kaasalainen et al. 2001) with a thermophysical model (Lagerros 1996, 1997, 1998). The asteroid's shape is parametrized by coefficients of spherical functions that describe a convex polyhedron of size D with typically hundreds of surface facets. For each facet, a 1-D heat diffusion equation is solved to compute its temperature and infrared flux at the time of observation. The surface's response to solar radiation is parametrized by the thermal inertia Γ, surface roughness (described by spherical craters), and light-scattering properties. Instead of using absolute magnitude, Bond albedo, and geometric albedo – which are properties unambiguously defined only for a sphere – we use Hapke's light-scattering model (Hapke 1981, 1984, 1986), from which any albedos can be directly computed. To tie the reflectance of the surface with the size of the asteroid, absolutely calibrated photometry is needed. Because most of the lightcurves we collected and observed are relative photometry, we also use the calibrated V-band photometry from the US Naval Observatory that covers a sufficiently wide range of solar phase angles. Parameters of Hapke's model can be optimized to fit the phase curve. The merit function that we minimize is a sum $\chi^2_{\rm VIS} + w\chi^2_{\rm IR}$ of χ^2 values for optical and thermal data. The relative weight w is iteratively set such that (in an ideal case) the fit to lightcurves is as good as without thermal data, and the fit to thermal data is good, i.e., the normalized $\chi^2_{\rm IR}$ is ~ 1.

[3] https://newton.spacedys.com/astdys2/index.php?pc=3.0

[4] https://ird.konkoly.hu/

4. Results

Table 3 summarises all the rotational and thermophysical properties of studied here targets. First the spin solution is presented, usually with its mirror counterpart, however in some cases the second solution gave bad fits and could safely be rejected. Lightcurve data are next described, with the quality of the fit to these data in the visible range. The second part of the table presents the thermal measurements from separate missions, and the radiometric diameter compared to WISE diameters from Mainzer et al. (2011); Masiero et al. (2011). We also cite taxonomic type after Bus & Binzel (2002a,b) and Tholen (1989) to enable consistency check with our values for geometric albedo (consistent in all cases, except for (923) Herluga), thermal inertia and the reduced χ^2 of modelled vs. observed fluxes. Lastly, the table contains the average heliocentric distance at which thermal measurements were taken, and thermal inertia reduced to one astronomical unit, using the formula:

$$\Gamma_{1AU} = \Gamma(r) r^{\alpha} \tag{1}$$

with the α exponent equal 0.75, to take into account a radiative conduction term in thermal conductivity. Different exponents would also be possible though, leading to wider range of Γ values at 1 AU, as shown by Alí-Lagoa et al. (2020).

In the Appendix we present the plots of χ^2 versus thermal inertia for various combinations of surface roughness and optimised size (Figures 4 - 19). For transforming various combinations of crater coverage and opening angle to rms of surface roughness we used the formula no. 20 from Lagerros (1998). For each target we also present the fit to WISE W3 and W4 lightcurves, whenever available (Figures 20 - 44). In some cases data in W3 band have been partially saturated, and could not be used here. Plots present the results for only one of two mirror pole solutions (the other pole gave very similarly results, as indicated by χ^2_{red} values from Table 3).

As a consistence test we re-run one of our previous targets, (478) Tergeste, now using a CITPM. In one of our earlier works (Marciniak et al. 2018) this target was spin and shape modelled, and next the resulting models best fitting the lightcurves in the visible were applied in TPM procedures. It then provided thermal inertia in the range of 30 - 120 SI units, and reduced χ^2 of models fit to infrared data of 2.18 and 1.53 for pole 1 and 2 respectively, showing strong preference of one of the spin and shape solutions, but also problems with fitting all thermal data. However, simultaneous optimisation on the same visible and infrared datasets led to somewhat different model. Most notably the reduced χ^2 decreased substantially to 0.65 for pole 1, and 0.84 for pole 2, so some preference for one spin solution remained, and thermal inertia shifted to smaller values: 1 - 50 SI units. For further check, this new shape models have been independently applied to classical TPM (code developed by Lagerros 1996, 1997, 1998) with best fitting thermal parameters, and the solution was confirmed with consistently low χ^2 of infrared data. The fit to visible lightcurves remained at similarly good level in both approaches, and the spin axis coordinates, size and albedo agreed within the errorbars with the original ones. Summing up,

it turned out that the CITPM method enabled finding much better combination of spin, shape and thermal parameters than the two-step approach used originally.

Other benefits from using CITPM revealed themselves when modelling targets like (487) Seppina and (666) Desdemona, that previously failed to provide robust solutions in classical TPM. With CITPM the unique and stable solution was found for 487, while for 666 thermal inertia still remained unconstrained, but at least the method enabled to constrain the size and albedo to a narrow range (see Table 3). In other cases ((667) Denise, (995) Sternberga) the convex inversion shape solutions had wrong inertia tensor (i.e. too much stretched along the spin axis), but thanks to the addition of calibrated data in the visible they gained correct proportions, with the "z" axis being the shortest axis of the shape model. Also, all the other targets shape models gained better constrained dimensions along the spin axis, which was frequent weakness of shape models based exclusively on relative photometry.

Additionally, for three targets of our sample there were good quality, multi-chord stellar occultations available in the PDS archive[5] (Herald et al. 2019, 2020). More recent occultation results were downloaded from the archive of the Occult programme[6]. We used them to independently scale obtained here shape models, using the method described in Ďurech et al. (2011), in order to compare obtained sizes with those from thermal fitting, confirm the shape silhouette, and if possible, identify the preferred pole solution. The results of occutation fitting are presented in Tab. 2, and in Figs. 1 - 3, showing the instantaneous silhouette of the shape model on the η, ξ sky plane scaled in kilometres. In all the figures north is up and west is right. The first model (pole 1) is shown with blue solid contour, and the second model with dashed magenta. Black lines in those figures mark occultation shadow chords calculated from occultation timings, with timing uncertainties shown at the extremities of each chord. The scale in seconds is given for reference as a red line. Negative (no occultation) chords are marked with dotted lines, while visual observations (as opposed to video or photoelectric) are marked with dashed lines. Table 5 in the Appendix lists the occultation observers and sites.

Some of our targets had spin and shape solutions already determined in the literature, in some cases only partial. In Table 1 we cite their spin axis coordinates and sidereal periods, if available, together with their reference. Comparison with our results in Table 3 shows general agreement, with the exception of (108) Hecuba model by Blanco & Riccioli (1998), (362) Havnia model by Wang et al. (2015), and (537) Pauly by Blanco et al. (2000) based on different shape approximations, which were not confirmed here. Italics mark the parameters strongly differing from the solutions obtained in this work. Within consistent solutions the difference in sidereal periods sometimes are of the order of a few 10^{-4} h, which seems small, but might be noticeable after a few apparitions. In the subsections below we focus on a few specific cases in more detail.

4.1. (362) Havnia

There were problems with some photometric data for this target. First, data obtained in 1978 by Harris & Young (1980), were published in the APC archive as a composite lightcurve, and with a wrong period of 18. hours. As a consequence, only one out of three lightcurves could be used, the one with original timings. This is general problem with some of early asteroid lightcurves in the archives, and special attention must be paid when using them. Another problems were caused by Super WASP data. Although in many cases these serendipitously gathered data are of great value, providing good lightcurves from desired geometries, in this case their intrinsic noise actually disabled finding a unique spin and shape solution. After removing most of Super WASP lightcurves for Havnia and keeping only five best ones (Fig. 62), the uniqueness of the solution greatly improved. Lightcurve inversion method is quite sensitive to the noise in the data.

Previously published by Wang et al. (2015) spin and shape model of Havnia was based on lightcurve inversion using Monte Carlo method on data from 4 apparitions (see Tab.1), while our model was based on (visible) lightcurves from 7 apparitions. Model by Wang et al. (2015) agrees with the model obtained here only in spin axis latitude (see Table 3), while the longitudes are substantially different. Sidereal periods might look similar at first sight, but actually they would lead to large divergence of extrema timings over just two apparitions.

In the thermal aspect our model is characterised by rather wide range of thermal inertia values due to poor infrared dataset (see N values in Table 3), but the plot 8 shows clear minimum around Γ=100. Unfortunately, all WISE W3 data had to be removed due to partial saturation. Even keeping only their best subset led to divergence.

There is a four-chord stellar occultation from the year 2017 available in the PDS archive. Both of our spin and shape solutions fit very well to this event, with all chords crossing close to the center of the body (see Fig. 1), resulting in volume-equivalent sizes a few percent smaller than the sizes from CITPM method (compare D values in Table 2, and 3). The small $\pm$1 km error in the occultation diameter is only a formal uncertainty determined via bootstrapping separate chords and repeating the fitting procedure multiple times. However the real uncertainty must be larger, due to the uncertainty of the shape model itself.

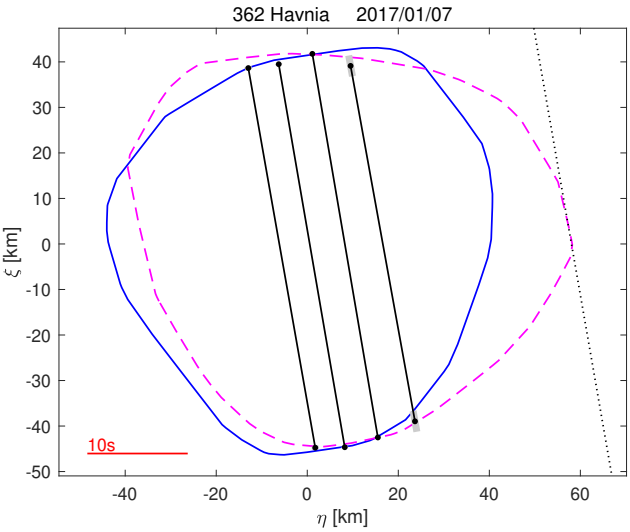

Fig. 1: CITPM shape models of asteroid (362) Havnia, fitted to a stellar occultation from 7. January 2017. At the end of each chord a timing uncertainty is marked. See Table 2 for diameters of equivalent volume spheres, and the text for plot interpretation.

[5] http://sbn.psi.edu/pds/resource/occ.html
[6] http://www.lunar-occultations.com/iota/occult4.htm

Table 1: Previously published spin parameters for targets studied here. The columns contain asteroid name, J2000 ecliptic coordinates λ_p, β_p of the spin solution, sidereal rotation period P, and the reference. Compare with the results in Table 3.

Asteroid	Pole		P	Reference
	$\lambda_p[^\circ]$	$\beta_p[^\circ]$	[hours]	
(108) Hecuba	*79* ± 1	*+13* ± 11	–	Blanco & Riccioli (1998)
	259 ± 7	*-6* ± 7	–	Blanco & Riccioli (1998)
(219) Thusnelda	*253* ± 4	-69 ± 4	59.712 ± 0.002	Ďurech et al. (2020)
(362) Havnia	96^{+3}_{-2}	$+39^{+7}_{-2}$	$16.918773^{+0.00003}_{0.000006}$	Wang et al. (2015)
	273^{+1}_{-6}	$+40^{+1}_{-10}$	$16.918935^{+0.00001}_{0.00004}$	Wang et al. (2015)
(478) Tergeste	2 ± 2	-42 ± 3	16.10308 ± 0.00003	Marciniak et al. (2018)
	216 ± 6	-56 ± 4	16.10308 ± 0.00003	Marciniak et al. (2018)
(483) Seppina	–	$+42 \pm 20$	12.72081 ± 0.00006	Ďurech et al. (2020)
(537) Pauly	*290* ± 31	$+40 \pm 31$	-	Blanco et al. (2000)
	31 ± 12	$+32 \pm 10$	16.2961 ± 0.0005	Hanuš et al. (2016)
	211 ± 16	$+51 \pm 10$	16.2961 ± 0.0005	Hanuš et al. (2016)
(552) Sigelinde	–	$+48 \pm 19$	17.1494 ± 0.0002	Ďurech et al. (2020)
(618) Elfriede	113 ± 3	$+54 \pm 3$	14.7952 ± 0.0001	Ďurech et al. (2020)
	323 ± 1	*+25* ± 3	14.7952 ± 0.0001	Ďurech et al. (2020)
(666) Desdemona	–	$+12 \pm 22$	14.6080 ± 0.0002	Ďurech et al. (2020)
(667) Denise	40 ± 6	-86 ± 3	12.6848 ± 0.0002	Ďurech et al. (2020)
(923) Herluga	188 ± 5	-60 ± 5	29.7282 ± 0.0007	Ďurech et al. (2020)

Target	Pole 1	Pole 2
362 Havnia	84 ± 1 km	88 ± 1 km
618 Elfriede	145 ± 7 km	155 ± 2 km
667 Denise	83 ± 2 km	rejected

Table 2: Diameters of equivalent volume spheres for CITPM shape models fitted to stellar occultations. Compare with radiometric diameters from CITPM in Table 3.

4.2. (537) Pauly

Previous spin and shape solutions for this asteroid have been published by Blanco et al. (2000), and by Hanuš et al. (2016). The results from the latter work are consistent with ours (see Tab. 3). Later, (537) Pauly has also been used in TPM via the model bootstrapping method (Hanuš et al. 2018). With this respect, our model of Pauly is made on many more dense lightcurves than that by Hanuš et al. (2016), and also richer thermal data (+ 9 AKARI points), and via simultaneous optimisation of both data types. Our size determinations (46 ± 2 km, and 47 ± 4 km) are somewhat larger than 40.7 ± 0.8 by Hanuš et al. (2018), but thermal inertia is similarly low, and albedo values also agree. Our χ^2 residuals are smaller than in the previous model (0.7 vs. 1.1) though. The difference in size might stem from the elongated shape of this target, and smaller set of infrared measurements, capturing the target at limited range of rotation phases, what might have led to underestimating the size in previous study.

4.3. (618) Elfriede

There were as many as four different stellar occultations by this target, containing from two to four chords. The fitting (Figs. 2) of our shape models to them seem to point to pole 2 solution ($\lambda_p = 341^\circ, \beta_p = +49^\circ$) as preferred one, but the preference is not very strong. The visual, southernmost chord in the first event probably has an underestimated duration.

In this case the occultation size agrees exactly for pole 1 with the radiometric size, while for pole 2 it is a few percent larger (see Tables 2 and 3), still within the range enabled by radiometric error bars. Our results, though self-consistent, are in disagreement with most of previous size determinations for 618 Elfriede. Occultation-determined size for pole 2 (155 ± 2 km) is almost 30% larger than AKARI (121.54 km) and IRAS (120.29 km) determinations (Usui et al. 2011; Tedesco et al. 2004), and 18% larger than diameter from WISE spacecraft (131.165 km Mainzer et al. 2011). In the case of determined here size for pole 1 the disagreement is less extreme: 20%, and 11% respectively, so agreeing with WISE diameter within the error bars. Summing up, since this work is the first comprehensive and multi-technique approach to this target (rich photometric set, simultaneously combined with infrared data from three missions, plus independent occultation fitting), then determined here size (145 - 155 km) can probably be considered the most reliable.

4.4. (667) Denise

For asteroid (667) Denise there were three good stellar occultations, with one containig as many as ten positive chords, thanks to a very successful European campaign (observers are listed in Table 5). Although both pole solutions are formally acceptable from the thermophysical point of view (both present in Table 3), the occultation fitting clearly enabled to reject the solution for pole 2 (see Fig. 3). Preferred pole 1 solution is thus marked with boldface in Table 3. The size determined from occultations (83 ± 2 km) is the same as the radiometric size (83^{+4}_{-2}).

5. Conclusions and future work

We fully characterised spin, shape, and thermal properties of 16 main belt asteroids, that have been previously neglected due to observing selection effects. Current set contains two updated models ((478) Tergeste, and (537) Pauly), and a few partial solutions with poorly determined thermal inertia, but other parameters well constrained. The multi-apparition targeted observing campaign together with good quality infrared data, espe-

cially from WISE spacectraft, led to consistent spin and shape models accompanied with precise size and albedo determinations, and thermal inertia determined for most of the targets for the first time. Thanks to simultaneous use of both visible and infarered data, our shape models are optimal in terms of reproducing well both types of data. Also, the Convex Inversion Thermophysical Model got more evidence supporting the robustness of the method, beyond the few cases studied originally.

With this work we substiantially increase the number of slow rotators with thermal inertia determined from detailed thermophysical modelling (over 40% incerase). It is neccessary to enlarge to pool of such well studied targets, so that investigations of separate groups and families could ultimately be performed, with possible linking thermal properties with surface material properties and family formation age (Harris & Drube 2020). Most of our presented here targets do not belong to any dynamical family (with the exception of 923 Herluga and 995 Sternebrga, both form Eunomia family, and also 618 Elfriede and 780 Armenia, each having their own small, compact family) so their low thermal inertia was to be expected, given their long collisional lifetime.

Our target sizes span the size range from a few tens to over 100 km, with most of the determinations being within 10% from previous determinations based on WISE data only, and simple thermal model. A few target sizes (e.g. 223 Rosa, 552 Sigelinde, 618 Elfriede) differ by more, yet current determinations, joining thermal data from three missions with a spin and shape model in detailed thermophysical modelling should be most reliable. Obtained albedo values agree with previously published taxonomic types.

Determined here thermal inertia values are for most of the targets below 100 SI units with preference for small values, indicating a presence of a thick layer of insulating regolith on most of these bodies. Thus, the hypothesis of thermal inertia growth with period (Harris & Drube 2016) is not confirmed here, similarly as in the works by (Marciniak et al. 2019) and Hanuš et al. (2018), while the rotation periods of our current targets range from 11 up to 59 hours. However, as found by Biele et al. (2019), and followed by Harris & Drube (2020), the uppermost fine-grained, highly porous surface layer of just a few millimetres thickness can hide the signatures of denser, more thermally conductive layers due to relatively small skin depth (d_s). Here, in spite of slow rotation, the d_s is mostly of the order of a few millimetres. The cases with poorly determined thermal inertia would yield d_s up to 3.5 cm, hovewer all the values below it are equally possible, so this cannot be used for drawing firm conclusions.

We also do not notice any correlation of thermal inertia with spin axis inclination, or any specific problems with fitting more inclined targets, that must experience seasonal cycles of heating and cooling. However, our thermal inertia determinations, as is often the case, are burdened with large uncertainties. It is possible that the trend linking thermal inertia and rotation period actually exists, but it eludes our studies, as precise thermal inertia determinations might be hampered by slow rotation, decreasing the thermal lag. For future studies it will be beneficial to focus on targets with thermal measurements from WISE spacecraft obtained at possibly largest span in time e.g. longer than 100 days, that should much better constrain thermal inertia, due to more varied viewing geometries, enabling comparison of thermal flux from e.g. pre- and post-opposition geometries.

Created here scaled spin and shape models with best fit thermal parameters are available at the new version of DAMIT database (Ďurech et al. 2010)[7], and data tables with photometry in the visible are available via the CDS archive.

[7] https://astro.troja.mff.cuni.cz/projects/damit/

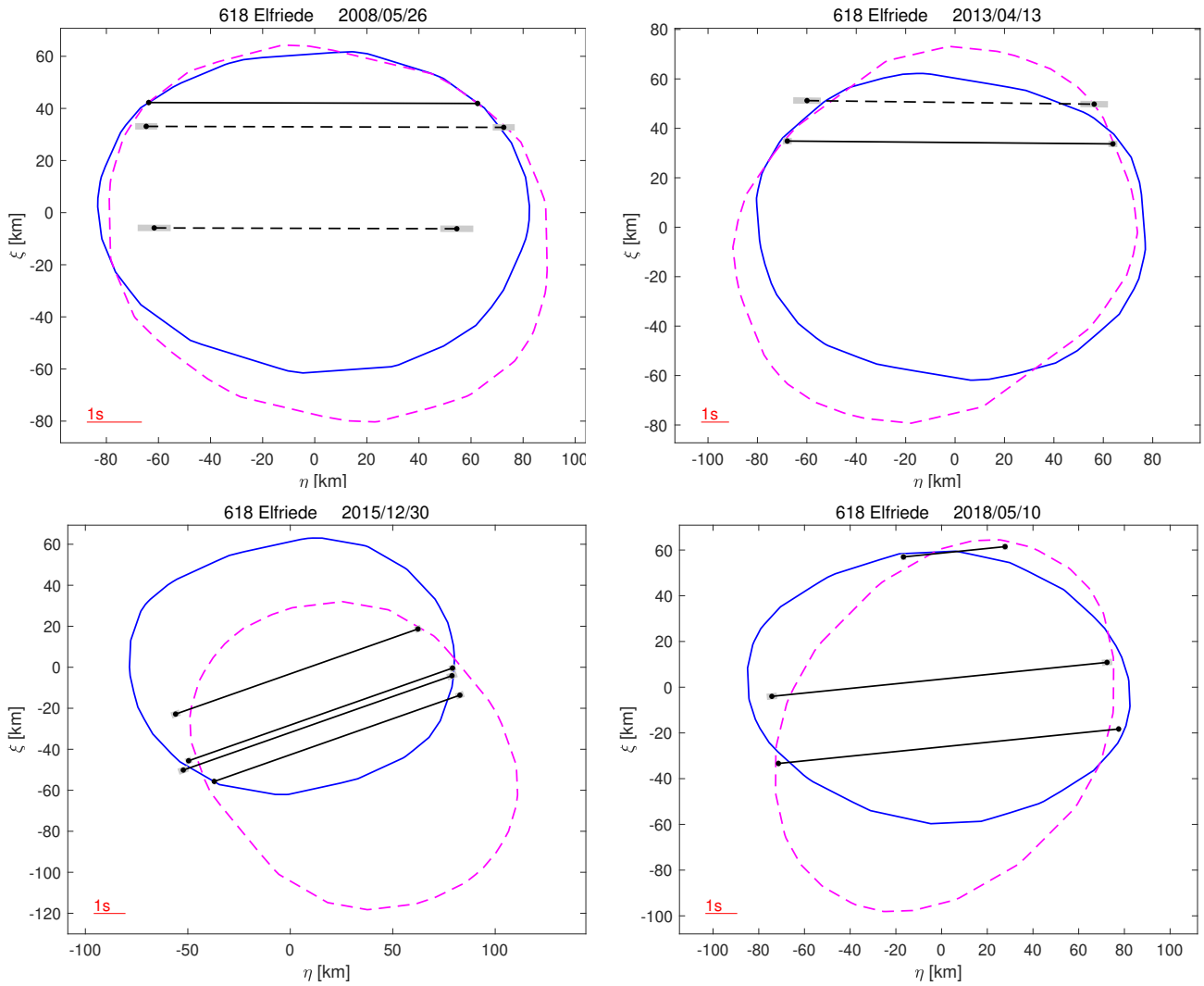

Fig. 2: CITPM shape models of (618) Elfriede, fitted to stellar occultations from 26. May 2008, 13. April 2013, 30 December 2015, and 10. May 2018. See Table 2 for diameters of equivalent volume spheres.

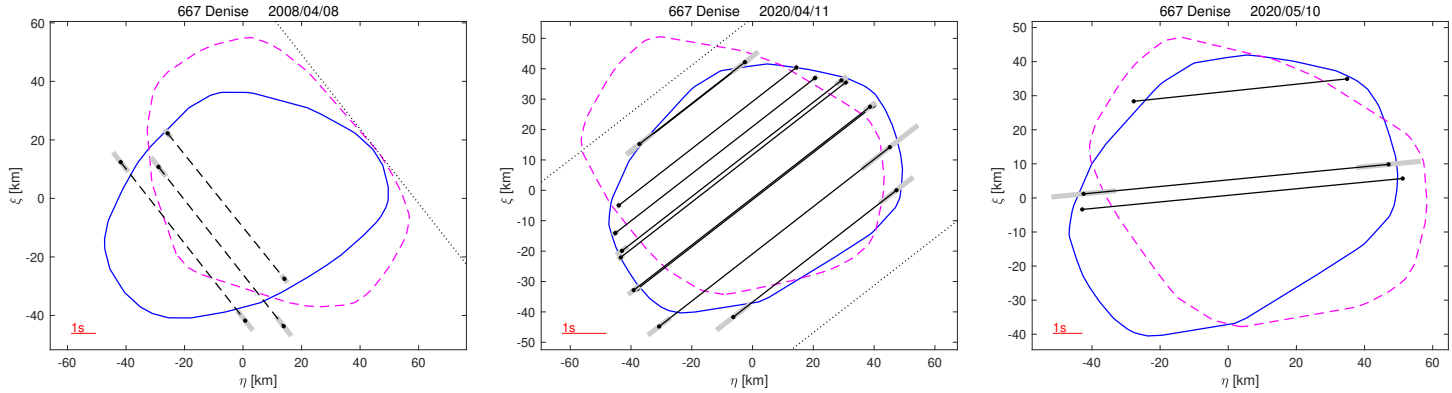

Fig. 3: CITPM shape models of (667) Denise fitted to stellar occultations from 8. April 2008, 11. April 2020, and 10. May 2020. Pole 1 solution (blue contour) is clearly preferred over pole1 (dashed magenta contour). See Table 2 for equivalent volume sphere diameter for the preferred pole solution.

Table 3: Spin parameters and thermophysical characteristics of asteroid models obtained in this work. For comparison diameters D_{WISE} from WISE spacecraft (Mainzer et al. 2011; Masiero et al. 2011) and taxonomic types are added (Bus & Binzel 2002a,b), and (Tholen 1989). The columns contain asteroid name, J2000 ecliptic coordinates λ_p, β_p of the spin solution, sidereal rotation period P, and the number of apparitions N_{app} during which the N_{lc} of visible lightcurves were obtained, followed by the deviation of model fit to those lightcurves (including fit to sparse data). Next part of the table details the infrared dataset: number of points provided by space observatories IRAS N_I, AKARI N_A, and WISE in W3 and W4 bands: N_{W3}, and N_{W4} respectively; and the radiometric solution for combined data: surface-equivalent size D, geometric albedo p_V, thermal inertia Γ in J m^{-2} s$^{-1/2}$ K^{-1} units, and the reduced chi-square of the best fit χ^2_{red}. Last two columns give mean heliocentric distance of thermal infrared observatons r_{hel}, and thermal inertia normalised to 1 AU Γ_{1AU}. Diameter in parentheses, due to lack of value from WISE, comes from IRAS survey results (Tedesco et al. 2004).

Asteroid	Pole		P	N_{app}	N_{lc}	vis. dev	N_I	N_A	N_{W3}	N_{W4}	D	D_{WISE}	Taxonomic	p_V	Γ	χ^2_{red}	r_{hel}	Γ_{1AU}
	$\lambda_p[^\circ]$	$\beta_p[^\circ]$	[hours]			[mag]					[km]	[km]	type		[SI units]	IR	[AU]	[SI units]
(108) Hecuba	181 ± 2	$+42 \pm 5$	14.25662 ± 0.00003	8	59	0.013	15	7	13	13	69^{+3}_{-1}	75.498	S	$0.24^{+0.04}_{-0.01}$	35^{+25}_{-30}	1.08	3.18	85
	352 ± 1	$+39 \pm 6$	14.25662 ± 0.00003	8	59	0.012	15	7	13	13	70 ± 2	75.498	S	$0.24^{+0.04}_{-0.01}$	40 ± 30	1.10	3.18	95
(202) Chryseis	94 ± 1	-49 ± 4	23.67025 ± 0.00006	7	70	0.012	7	8		12	90^{+4}_{-3}	97.948	S	$0.22^{+0.03}_{-0.01}$	< 180	0.35	2.96	< 405
	261 ± 1	-34 ± 4	23.67028 ± 0.00004	7	70	0.012	7	8		12	90^{+3}_{-3}	97.948	S	$0.22^{+0.01}_{-0.01}$	< 180	0.36	2.96	< 405
(219) Thusnelda	300 ± 10	-66 ± 10	59.7105 ± 0.0001	6	116	0.014	18	6		19	44^{+2}_{-4}	38.078	S	$0.19^{+0.04}_{-0.01}$	< 120	0.80	2.28	< 185
(223) Rosa	22 ± 3	$+18 \pm 18$	20.2772 ± 0.0003	7	58	0.012	20	5		12	69^{+9}_{-3}	83.394	X	$0.033^{+0.006}_{-0.004}$	< 300	0.72	2.99	< 230
	203 ± 2	$+26 \pm 15$	20.2769 ± 0.0003	7	58	0.012	20	5		12	70^{+6}_{-2}	83.394	X	$0.032^{+0.007}_{-0.003}$	< 300	0.78	2.99	< 230
(362) Havnia	14 ± 2	$+33 \pm 2$	16.92665 ± 0.00003	7	38	0.017		9		13	92^{+6}_{-5}	89.202	XC	$0.044^{+0.006}_{-0.004}$	< 180	0.80	2.64	< 370
	208 ± 8	$+35 \pm 4$	16.92668 ± 0.00003	7	38	0.017		9		13	91^{+8}_{-3}	89.202	XC	$0.046^{+0.004}_{-0.008}$	< 200	0.67	2.64	< 410
(478) Tergeste	2 ± 5	-38 ± 8	16.10308 ± 0.00004	6	48	0.019	27	8	9	9	83 ± 4	84.975	S	$0.16^{+0.05}_{-0.01}$	2^{+45}_{-1}	0.94	3.12	5
	216 ± 7	-62 ± 4	16.10312 ± 0.00004	6	48	0.016	27	8	9	9	81^{+5}_{-4}	84.975	S	$0.18^{+0.03}_{-0.02}$	26 ± 25	0.88	3.12	60
(483) Seppina	127 ± 3	$+47 \pm 3$	12.720968 ± 0.000004	8	56	0.019	34	12	12	12	73^{+5}_{-2}	84.975	S	$0.16^{+0.04}_{-0.01}$	17^{+23}_{-12}	0.80	3.46	45
	356 ± 4	$+60 \pm 3$	12.720977 ± 0.000002	8	56	0.019	34	12	12	12	74^{+4}_{-2}	84.975	S	$0.16^{+0.04}_{-0.01}$	23^{+17}_{-18}	0.83	3.46	60
(501) Urhixidur	49 ± 40	$+84 \pm 12$	13.17203 ± 0.00002	7	61	0.019	11	8	11	11	77^{+5}_{-2}	85.404	C	$0.051^{+0.003}_{-0.008}$	4^{+35}_{-2}	0.53	3.24	10
	262 ± 24	$+66 \pm 11$	13.17203 ± 0.00001	7	61	0.018	11	8	11	11	82^{+2}_{-4}	85.404	C	$0.050^{+0.002}_{-0.007}$	13^{+30}_{-11}	0.53	3.24	31
(537) Pauly	32 ± 3	$+43 \pm 6$	16.29601 ± 0.00002	7	50	0.018	8	9	6	6	47^{+1}_{-2}	52.330	DU	$0.26^{+0.03}_{-0.02}$	11^{+30}_{-10}	0.70	3.18	26
	214 ± 4	$+60 \pm 9$	16.29597 ± 0.00001	7	50	0.018	8	9	6	6	46 ± 2	52.300	DU	$0.25^{+0.05}_{-0.02}$	13^{+50}_{-12}	0.74	3.18	31
(552) Sigelinde	8 ± 24	$+73 \pm 9$	17.14963 ± 0.00001	6	65	0.017	8	6	4		88^{+10}_{-5}	(77.56)	C	$0.030^{+0.011}_{-0.007}$	3^{+55}_{-2}	0.97	3.26	7
	189 ± 18	$+60 \pm 17$	17.14962 ± 0.00003	6	65	0.017	8	6	4		91^{+7}_{-13}	(77.56)	C	$0.029^{+0.005}_{-0.007}$	2^{+55}_{-1}	1.13	3.26	5
(618) Elfriede	102 ± 20	$+64 \pm 7$	14.79565 ± 0.00002	9	68	0.015	17	5		12	145^{+15}_{-13}	131.165	C	$0.047^{+0.010}_{-0.003}$	< 350	0.28	3.32	< 860
	341 ± 13	$+49 \pm 6$	14.79564 ± 0.00002	9	68	0.015	17	5		12	146^{+15}_{-16}	131.165	C	$0.053^{+0.002}_{-0.009}$	< 400	0.32	3.32	< 980
(666) Desdemona	10 ± 4	$+39 \pm 5$	14.60795 ± 0.00008	7	60	0.022	21	5	13	13	$28.4^{+0.9}_{-0.8}$	31.485	S	$0.111^{+0.007}_{-0.009}$	< 70	0.83	2.79	< 150
	174 ± 3	$+36 \pm 11$	14.60796 ± 0.00003	7	60	0.022	21	5	13	13	$28.3^{+0.9}_{-1.0}$	31.485	S	$0.116^{+0.002}_{-0.014}$	< 100	0.77	2.79	< 215
(667) Denise	**15 ± 25**	**-83 ± 6**	**12.68499 ± 0.00003**	5	40	0.024	21	5	15	13	83^{+4}_{-2}	88.630	C	0.051 ± 3	13^{+17}_{-8}	1.19	3.36	32
	237 ± 3	-23 ± 6	12.68497 ± 0.00003	5	40	0.025	21	5	15	13	82^{+5}_{-2}	88.630	C	$0.051^{+0.002}_{-0.004}$	6^{+24}_{-1}	1.16	3.36	15
(780) Armenia	144 ± 7	-44 ± 11	19.88453 ± 0.00007	8	95	0.014	24	7		12	98^{+2}_{-3}	102.257	C	$0.042^{+0.005}_{-0.003}$	< 300	0.47	2.98	< 680
	293 ± 3	-23 ± 6	19.88462 ± 0.00009	8	95	0.015	24	7		12	102^{+3}_{-2}	102.257	C	0.038 ± 0.003	< 250	0.63	2.98	< 570
(923) Herluga	218 ± 9	-68 ± 5	29.72820 ± 0.00002	7	51	0.022	12	8	16	16	$36.2^{+0.4}_{-1.5}$	37.638	C	$0.047^{+0.004}_{-0.003}$	37^{+15}_{-36}	0.92	2.73	80
	334 ± 7	-52 ± 3	29.72826 ± 0.00001	7	51	0.023	12	8	16	16	$34.1^{+0.8}_{-1.0}$	37.638	C	$0.050^{+0.002}_{-0.003}$	14^{+35}_{-13}	0.95	2.73	30
(995) Sternberga	27 ± 3	-20 ± 6	11.19511 ± 0.00012	7	81	0.019	22	6	11	11	$25.5^{+1.1}_{-1.4}$	22.350	S	$0.22^{+0.03}_{-0.04}$	< 100	0.85	2.56	< 200
	222 ± 4	-26 ± 5	11.19512 ± 0.00008	7	81	0.019	22	6	11	11	$25.2^{+1.1}_{-0.9}$	22.350	S	$0.226^{+0.005}_{-0.032}$	< 120	0.84	2.56	< 240

Acknowledgements. This work was was initiated with the support from the National Science Centre, Poland, through grant no. 2014/13/D/ST9/01818; and from the European Union's Horizon 2020 Research and Innovation Programme, under Grant Agreement no 687378 (SBNAF). The work of JD was supported by the grant 20-08218S of the Czech Science Foundation.
The Joan Oró Telescope (TJO) of the Montsec Astronomical Observatory (OAdM) is owned by the Catalan Government and operated by the Institute for Space Studies of Catalonia (IEEC). This article is based on observations made in the Observatorios de Canarias del IAC with the 0.82m IAC80 telescope operated on the island of Tenerife by the Instituto de Astrofísica de Canarias (IAC) in the Observatorio del Teide. This article is based on observations made with the SARA telescopes (Southeastern Association for Research in Astronomy), whose nodes are located at the Observatorios de Canarias del IAC on the island of La Palma in the Observatorio del Roque de los Muchachos; Kitt Peak, AZ under the auspices of the National Optical Astronomy Observatory (NOAO); and Cerro Tololo Inter-American Observatory (CTIO) in La Serena, Chile. This project uses data from the SuperWASP archive. The WASP project is currently funded and operated by Warwick University and Keele University, and was originally set up by Queen's University Belfast, the Universities of Keele, St. Andrews, and Leicester, the Open University, the Isaac Newton Group, the Instituto de Astrofisica de Canarias, the South African Astronomical Observatory, and by STFC.
Funding for the Kepler and K2 missions are provided by the NASA Science Mission Directorate. The data presented in this paper were obtained from the Mikulski Archive for Space Telescopes (MAST). STScI is operated by the Association of Universities for Research in Astronomy, Inc., under NASA contract NAS5- 26555. Support for MAST for non-HST data is provided by the NASA Office of Space Science via grant NNX09AF08G and by other grants and contracts.
We acknowledge the contributions of the occultation observers who have provided the observations in the data-set. Most of those observers are affiliated with one or more of: European Asteroidal Occultation Network (EAON), International Occultation Timing Association (IOTA), International Occultation Timing Association European Section (IOTAES), Japanese Occultation Information Network (JOIN), Trans Tasman Occultation Alliance (TTOA).

References

Alí-Lagoa, V., Müller, T. G., Kiss, C., et al. 2020, A&A, 638, A84
Barucci, M. A., di Martino, M., & Fulchignoni, M. 1992, AJ, 103, 1679
Benishek, V. & Pilcher, F. 2009, Minor Planet Bulletin, 36, 167
Biele, J., Kührt, E., Senshu, H., et al. 2019, Progress in Earth and Planetary Science, 6, 48
Blanco, C., Cigna, M., & Riccioli, D. 2000, Planet. Space Sci., 48, 973
Blanco, C. & Riccioli, D. 1998, A&AS, 131, 385
Brinsfield, J. W. 2009, Minor Planet Bulletin, 36, 64
Bus, S. J. & Binzel, R. P. 2002a, Icarus, 158, 146
Bus, S. J. & Binzel, R. P. 2002b, Icarus, 158, 106
Delbo, M., Libourel, G., Wilkerson, J., et al. 2014, Nature, 508, 233
Ďurech, J., Delbo', M., Carry, B., Hanuš, J., & Alí-Lagoa, V. 2017, A&A, 604, A27
Ďurech, J., Sidorin, V., & Kaasalainen, M. 2010, A&A, 513, A46
Ďurech, J., Tonry, J., Erasmus, N., et al. 2020, A&A, 643, A59
Egan, M. P., Price, S. D., & Kraemer, K. E. 2003, in American Astronomical Society Meeting Abstracts, Vol. 203, American Astronomical Society Meeting Abstracts, 57.08
Grice, J., Snodgrass C., Green S., Parley N., & Carry, B. 2017, in Asteroids, Comets, meteors: ACM 2017
Gundlach, B. & Blum, J. 2013, Icarus, 223, 479
Hanuš, J., Delbo', M., Ďurech, J., & Alí-Lagoa, V. 2018, Icarus, 309, 297
Hanuš, J., Ďurech, J., Brož, M., et al. 2011, A&A, 530, A134
Hanuš, J., Ďurech, J., Oszkiewicz, D. A., et al. 2016, A&A, 586, A108
Hapke, B. 1981, J. Geophys. Res., 86, 3039
Hapke, B. 1984, Icarus, 59, 41
Hapke, B. 1986, Icarus, 67, 264
Harris, A. W. & Drube, L. 2016, ApJ, 832, 127
Harris, A. W. & Drube, L. 2020, ApJ, 901, 140
Harris, A. W. & Young, J. W. 1980, Icarus, 43, 20
Harris, A. W., Young, J. W., Dockweiler, T., et al. 1992, Icarus, 95, 115
Herald, D., Frappa, E., Gault, D., et al. 2019, Asteroid Occultations V3.0, NASA Planetary Data System
Herald, D., Gault, D., Anderson, R., et al. 2020, MNRAS, 499, 4570
Howell, S. B., Sobeck, C., Haas, M., et al. 2014, Publications of the Astronomical Society of the Pacific, 126, 398
Kaasalainen, M. & Durech, J. 2020, arXiv e-prints, arXiv:2005.09947
Kaasalainen, M., Torppa, J., & Muinonen, K. 2001, Icarus, 153, 37
Keihm, S., Tosi, F., Kamp, L., et al. 2012, Icarus, 221, 395
Klinglesmith, Daniel A., I., Hendrickx, S., Kimber, C., & Madden, K. 2017, Minor Planet Bulletin, 44, 244
Lagerkvist, C. I. & Kamel, L. 1982, Moon and Planets, 27, 463
Lagerkvist, C. I., Magnusson, P., Debehogne, H., et al. 1992, A&AS, 95, 461
Lagerros, J. S. V. 1996, A&A, 310, 1011
Lagerros, J. S. V. 1997, A&A, 325, 1226
Lagerros, J. S. V. 1998, A&A, 332, 1123
Mainzer, A., Grav, T., Masiero, J., et al. 2011, ApJ, 741, 90
Marciniak, A., Alí-Lagoa, V., Müller, T. G., et al. 2019, A&A, 625, A139
Marciniak, A., Bartczak, P., Müller, T., et al. 2018, A&A, 610, A7
Marciniak, A., Pilcher, F., Oszkiewicz, D., et al. 2015, Planet. Space Sci., 118, 256
Masiero, J. R., Mainzer, A. K., Grav, T., et al. 2011, ApJ, 741, 68
Murakami, H., Baba, H., Barthel, P., et al. 2007, PASJ, 59, S369
Neugebauer, G., Habing, H. J., van Duinen, R., et al. 1984, ApJ, 278, L1
Oey, J. 2009, Minor Planet Bulletin, 36, 4
Okada, T., Fukuhara, T., Tanaka, S., et al. 2020, Nature, 579, 518
Pál, A., Szakáts, R., Kiss, C., et al. 2020, ApJS, 247, 26
Pilcher, F. 2012, Minor Planet Bulletin, 39, 171
Pilcher, F. 2013, Minor Planet Bulletin, 40, 158
Pilcher, F. 2014, Minor Planet Bulletin, 41, 250
Rozitis, B., Maclennan, E., & Emery, J. P. 2014, Nature, 512, 174
Stephens, R. D. 2009, Minor Planet Bulletin, 36, 157
Stephens, R. D. 2013, Minor Planet Bulletin, 40, 34
Stephens, R. D., Pilcher, F., Hamanowa, H., Hamanowa, H., & Ferrero, A. 2011, Minor Planet Bulletin, 38, 208
Szakáts, R., Müller, T., Alí-Lagoa, V., et al. 2020, A&A, 635, A54
Tedesco, E. F., Noah, P. V., Noah, M., & Price, S. D. 2004, NASA Planetary Data System, IRAS
Tholen, D. J. 1989, in Asteroids II, ed. R. P. Binzel, T. Gehrels, & M. S. Matthews, 1139–1150
Usui, F., Kuroda, D., Müller, T. G., et al. 2011, PASJ, 63, 1117
Ďurech, J., Kaasalainen, M., Herald, D., et al. 2011, Icarus, 214, 652
Vokrouhlický, D., Bottke, W. F., Chesley, S. R., Scheeres, D. J., & Statler, T. S. 2015, Asteroids IV, ed. P. Michel, F. E. DeMeo, & W. F. Bottke, 509–531
Walsh, K. J., Jawin, E. R., Ballouz, R. L., et al. 2019, Nature Geoscience, 12, 242
Wang, X., Muinonen, K., & Wang, Y. 2015, Planet. Space Sci., 118, 242
Warner, B. D. 2006, Minor Planet Bulletin, 33, 85
Warner, B. D. 2007a, Minor Planet Bulletin, 34, 72
Warner, B. D. 2007b, Minor Planet Bulletin, 34, 104
Waszczak, A., Chang, C.-K., Ofek, E. O., et al. 2015, AJ, 150, 75
Weidenschilling, S. J., Chapman, C. R., Davis, D. R., et al. 1990, Icarus, 86, 402
Wright, E. L., Eisenhardt, P. R. M., Mainzer, A. K., et al. 2010, AJ, 140, 1868
Zappalà, V., Di Martino, M., Cellino, A., et al. 1989, Icarus, 82, 354

Appendix A

This section contains:
Plots of χ^2 versus thermal inertia for various combinations of surface roughness and optimised size (Figures 4 - 19).
Thermal lightcurves fit to the model (Figures 20 - 44).
Details of all lightcurve observations used for the modelling (Table 4).
List of stellar occultation observers and sites (Table5).
Composite lightcurves presenting new data of target asteroids (Figures 45 - 110).

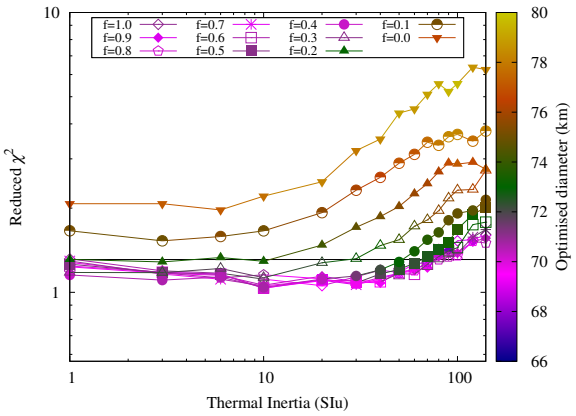

Fig. 4: Reduced χ^2 values vs. thermal inertia for various combinations of surface roughness (symbol coded) and optimised diameters (colour coded) for asteroid (108) Hecuba.

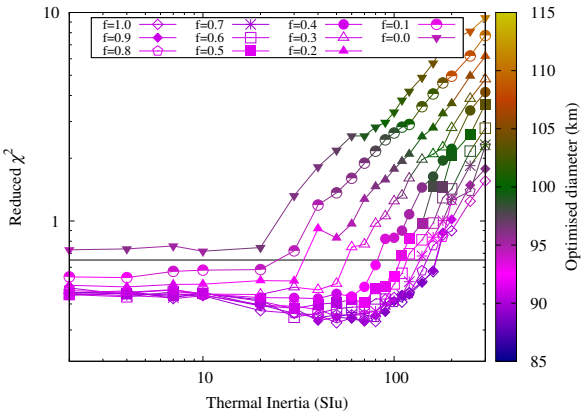

Fig. 5: Reduced χ^2 values vs. thermal inertia for (202) Chryseis

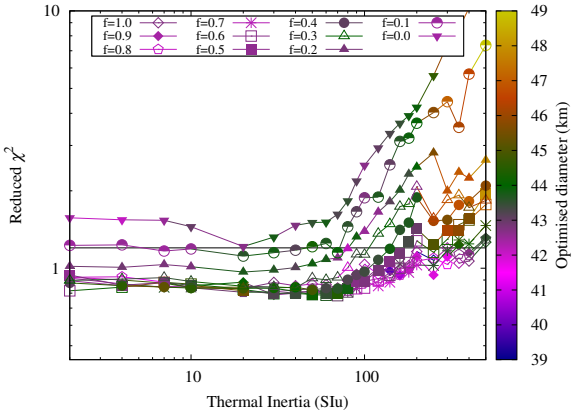

Fig. 6: Reduced χ^2 values vs. thermal inertia for (219) Thusnelda

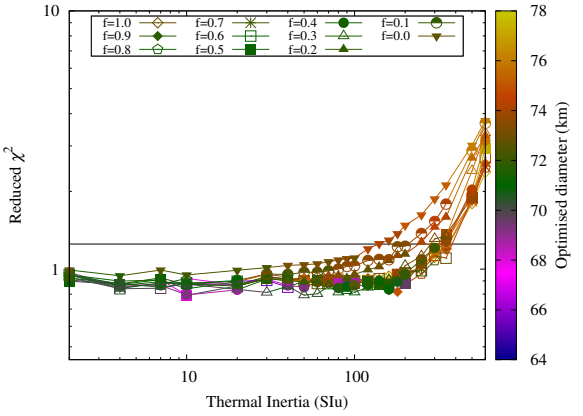

Fig. 7: Reduced χ^2 values vs. thermal inertia for (223) Rosa

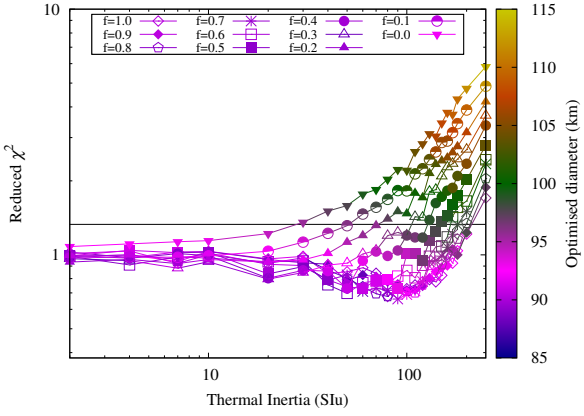

Fig. 8: Reduced χ^2 values vs. thermal inertia for (362) Havnia

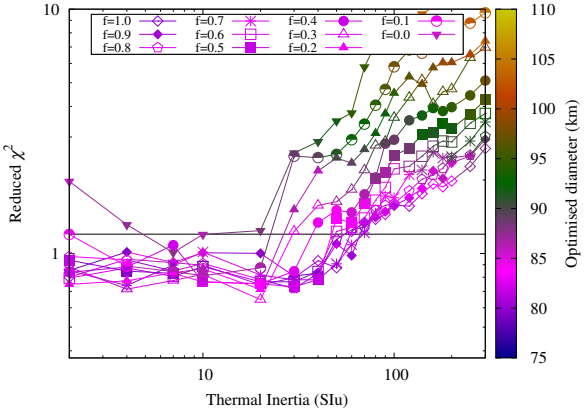

Fig. 9: Reduced χ^2 values vs. thermal inertia for (478) Tergeste

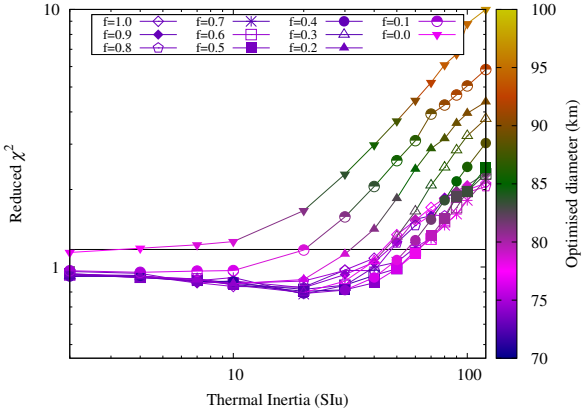

Fig. 10: Reduced χ^2 values vs. thermal inertia for (483) Seppina

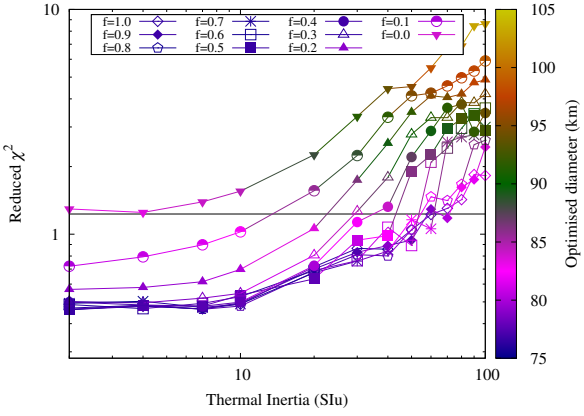

Fig. 11: Reduced χ^2 values vs. thermal inertia for (501) Urhixidur

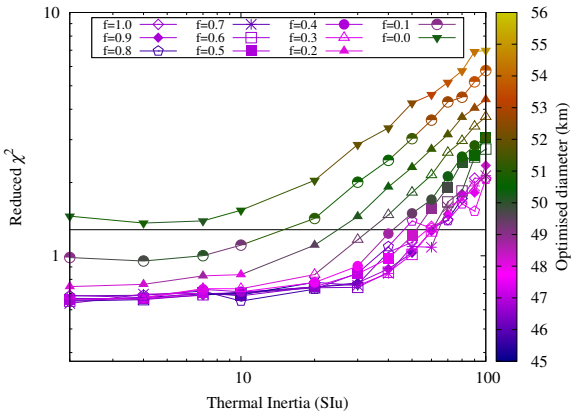

Fig. 12: Reduced χ^2 values vs. thermal inertia for (537) Pauly

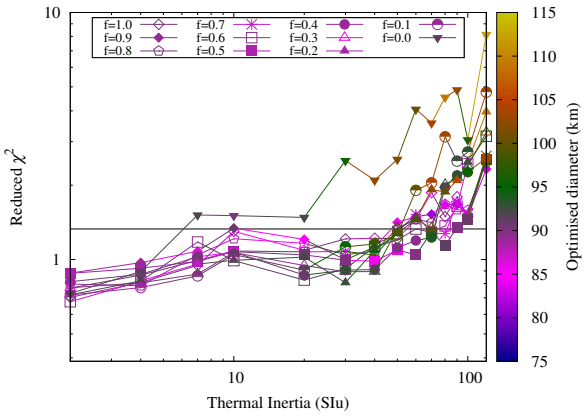

Fig. 13: Reduced χ^2 values vs. thermal inertia for (552) Sigelinde

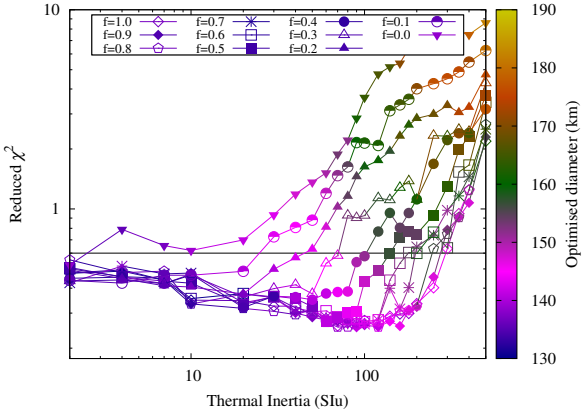

Fig. 14: Reduced χ^2 values vs. thermal inertia for (618) Elfriede

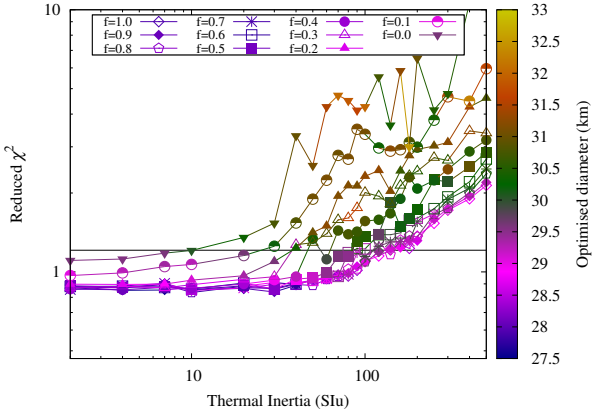

Fig. 15: Reduced χ^2 values vs. thermal inertia for (666) Desdemona

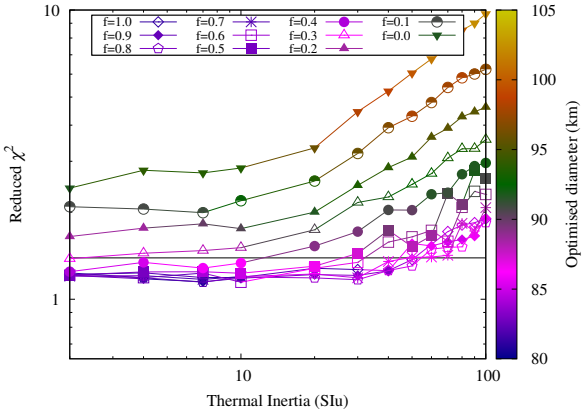

Fig. 16: Reduced χ^2 values vs. thermal inertia for (667) Denise

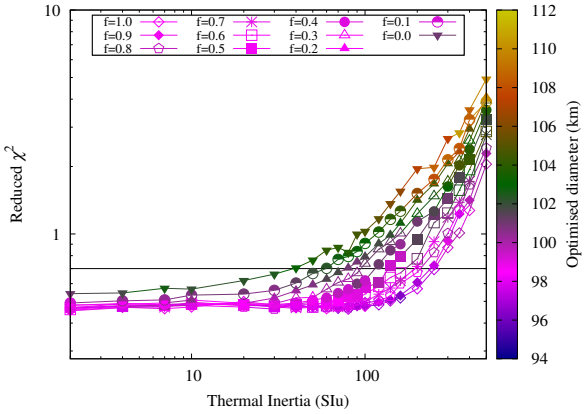

Fig. 17: Reduced χ^2 values vs. thermal inertia for (780) Armenia

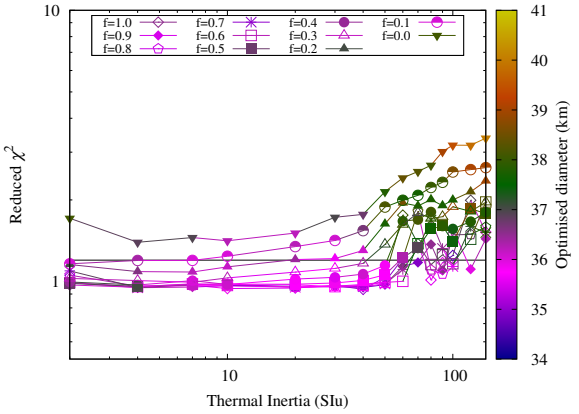

Fig. 18: Reduced χ^2 values vs. thermal inertia for (923) Herluga

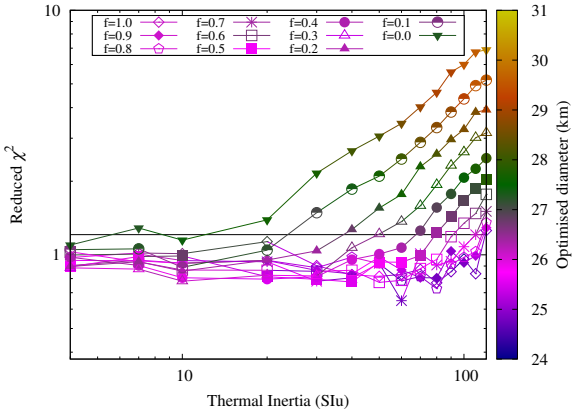

Fig. 19: Reduced χ^2 values vs. thermal inertia for (995) Sternberga

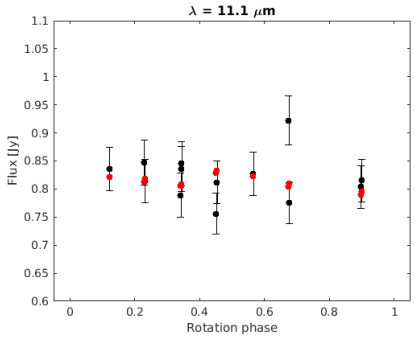

Fig. 20: Infrared model fluxes (red circles) compared to measured fluxes in W3 band of WISE spacecraft (black circles) for asteroid (108) Hecuba.

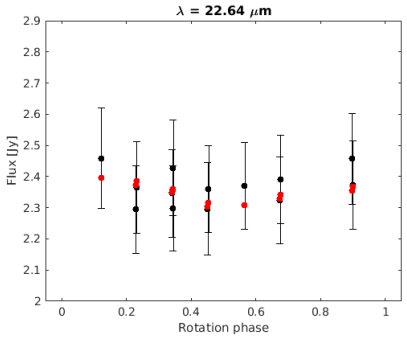

Fig. 21: Infrared model fluxes compared to measured fluxes in W4 band of WISE spacecraft for asteroid (108) Hecuba.

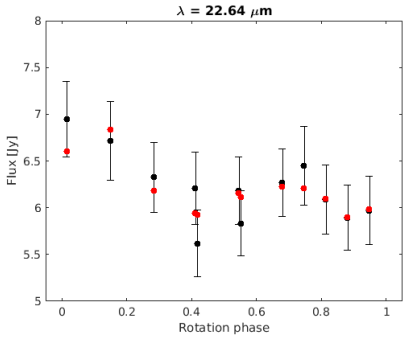

Fig. 22: Infrared model fluxes compared to measured fluxes in W4 band of WISE spacecraft for asteroid (202) Chryseis.

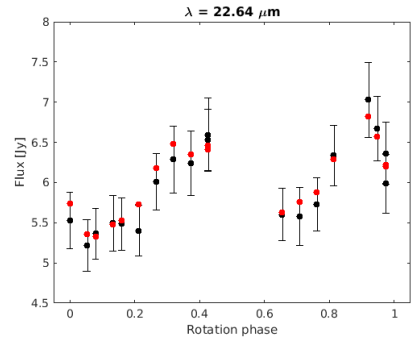

Fig. 23: Infrared model fluxes compared to measured fluxes in W4 band of WISE spacecraft for asteroid (219) Thusnelda.

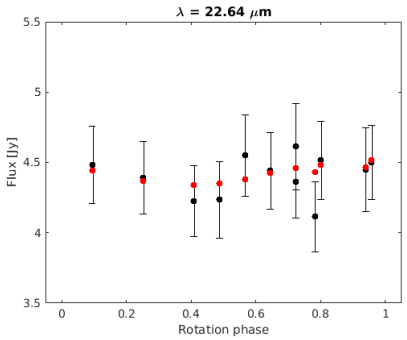

Fig. 24: Infrared model fluxes compared to measured fluxes in W4 band of WISE spacecraft for asteroid (223) Rosa.

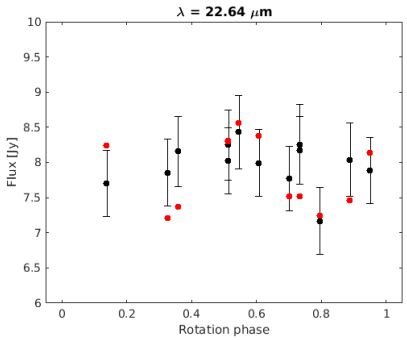

Fig. 25: Infrared model fluxes compared to measured fluxes in W4 band of WISE spacecraft for asteroid (362) Havnia.

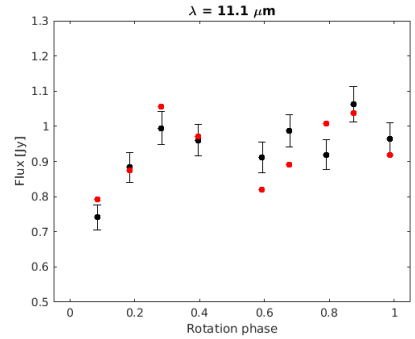

Fig. 26: Infrared model fluxes compared to measured fluxes in W3 band of WISE spacecraft for asteroid (478) Tergeste.

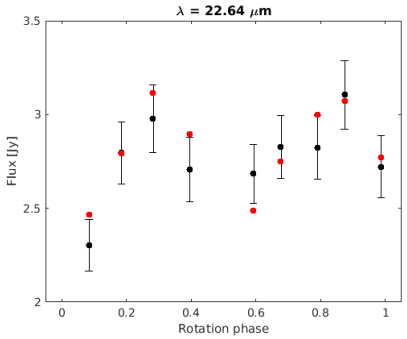

Fig. 27: Infrared model fluxes compared to measured fluxes in W4 band of WISE spacecraft for asteroid (478) Tergeste.

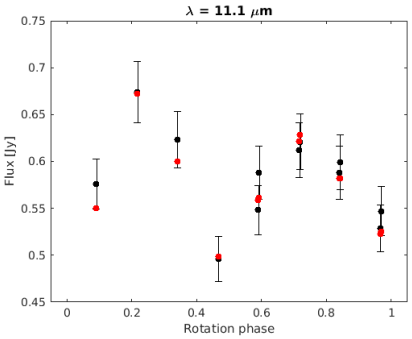

Fig. 28: Infrared model fluxes compared to measured fluxes in W3 band of WISE spacecraft for asteroid (483) Seppina.

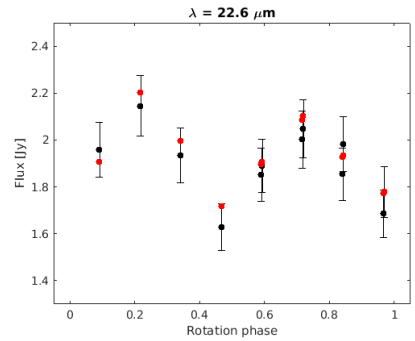

Fig. 29: Infrared model fluxes compared to measured fluxes in W4 band of WISE spacecraft for asteroid (483) Seppina.

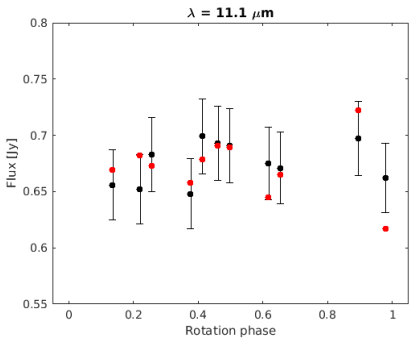

Fig. 30: Infrared model fluxes compared to measured fluxes in W3 band of WISE spacecraft for asteroid (501) Urhixidur.

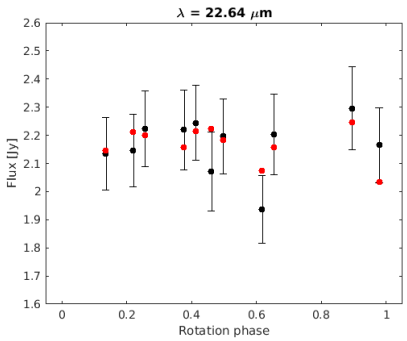

Fig. 31: Infrared model fluxes compared to measured fluxes in W4 band of WISE spacecraft for asteroid (501) Urhixidur.

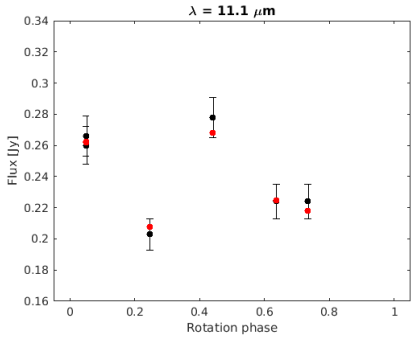

Fig. 32: Infrared model fluxes compared to measured fluxes in W3 band of WISE spacecraft for asteroid (537) Pauly.

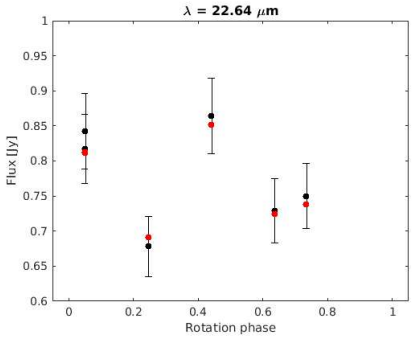

Fig. 33: Infrared model fluxes compared to measured fluxes in W4 band of WISE spacecraft for asteroid (537) Pauly.

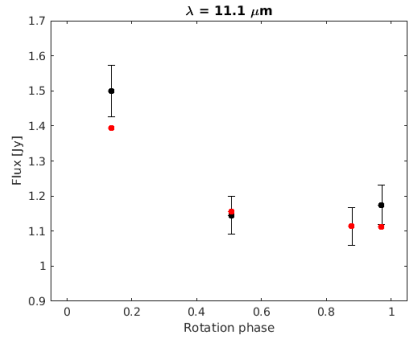

Fig. 34: Infrared model fluxes compared to measured fluxes in W3 band of WISE spacecraft for asteroid (552) Sigelinde.

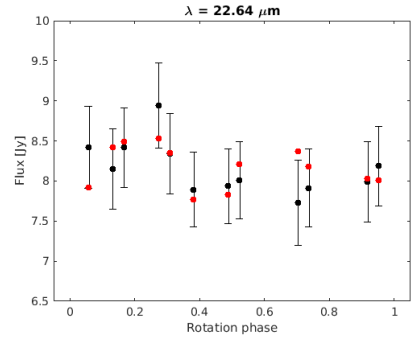

Fig. 35: Infrared model fluxes compared to measured fluxes in W4 band of WISE spacecraft for asteroid (618) Elfriede.

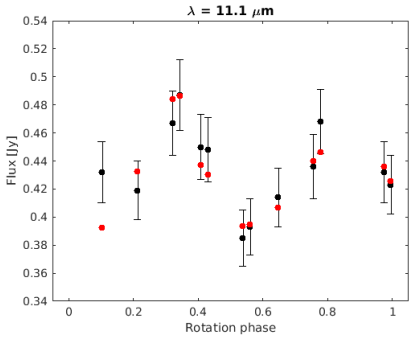

Fig. 36: Infrared model fluxes compared to measured fluxes in W3 band of WISE spacecraft for asteroid (666) Desdemona.

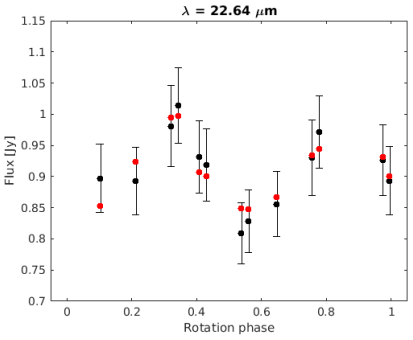

Fig. 37: Infrared model fluxes compared to measured fluxes in W4 band of WISE spacecraft for asteroid (666) Desdemona.

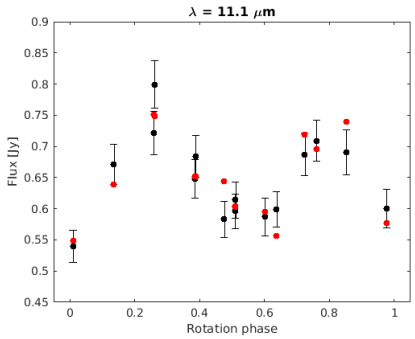

Fig. 38: Infrared model fluxes compared to measured fluxes in W3 band of WISE spacecraft for asteroid (667) Denise.

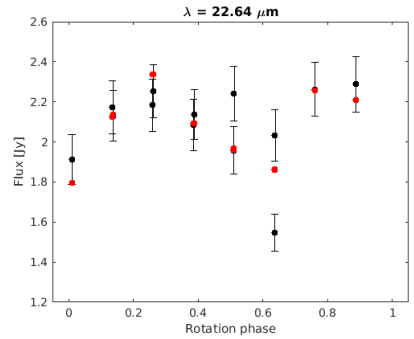

Fig. 39: Infrared model fluxes compared to measured fluxes in W4 band of WISE spacecraft for asteroid (667) Denise.

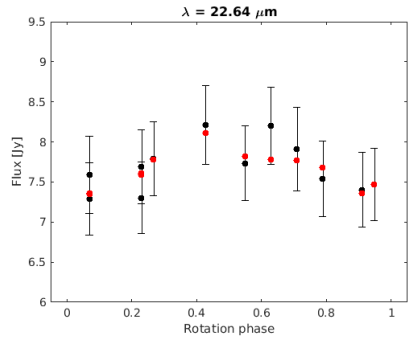

Fig. 40: Infrared model fluxes compared to measured fluxes in W3 band of WISE spacecraft for asteroid (780) Armenia.

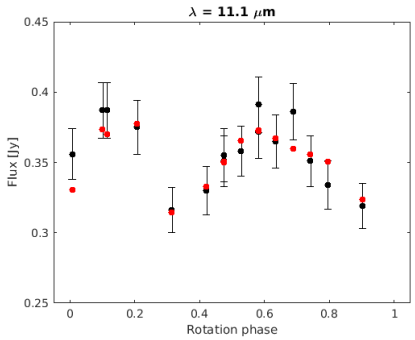

Fig. 41: Infrared model fluxes compared to measured fluxes in W3 band of WISE spacecraft for asteroid (923) Herluga.

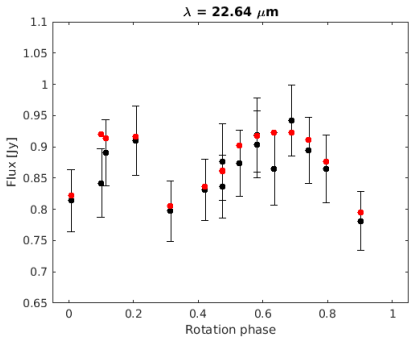

Fig. 42: Infrared model fluxes compared to measured fluxes in W4 band of WISE spacecraft for asteroid (923) Herluga.

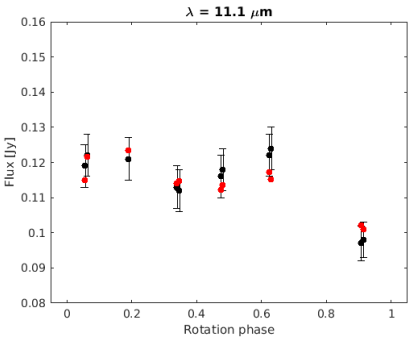

Fig. 43: Infrared model fluxes compared to measured fluxes in W3 band of WISE spacecraft for asteroid (995) Sternberga.

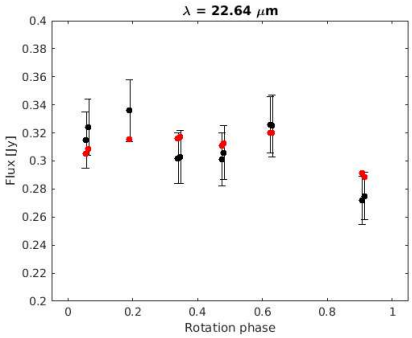

Fig. 44: Infrared model fluxes compared to measured fluxes in W4 band of WISE spacecraft for asteroid (995) Sternberga.

Table 4: Details of all visible photometric observations: observing dates, number of lightcurves, ecliptic longitude of the target, sun-target-observer phase angle, observer's name (or paper citation in case of published data), and the observing site. Some data come from robotic telescopes, so they have no observer specified. In case of data from TESS spacecraft the number of lightcurves denotes the number of days of continuous observations.

Date	N_{lc}	λ [deg]	Phase angle [deg]	Observer	Site
(108) Hecuba					
2007 03 04 - 2007 03 09	5	126	11 - 12	Warner (2007a)	CSSS - Palmer Divide Station, USA
2011 11 30	1	68	2	T. Kundera	Suhora, Poland
2012 01 23 - 2012 03 05	7	61 - 66	15 - 17	Waszczak et al. (2015)	PTF, USA
2012 12 27 - 2013 02 26	8	140 - 149	2 - 14	Pilcher (2013)	Organ Mesa, USA
2014 04 20 - 2014 04 17	9	225 - 230	2 - 6	Pilcher (2014)	Organ Mesa, USA
2015 07 02	1	310	9	A. Marciniak	Teide, Spain
2015 08 05 - 2015 08 07	3	304	3 - 5	M. Żejmo	Adiyaman, Turkey
2015 08 10 - 2015 09 13	6	299 - 303	5 - 14	-	Montsec, Spain
2016 08 28 - 2017 01 08	7	7 - 19	7 - 16	A. Marciniak, R. Hirsch, K. Żukowski, M. Butkiewicz - Bąk	Borowiec, Poland
2017 11 03 - 2017 11 15	5	85 - 86	9 - 12	-	Montsec, Spain
2018 02 28 - 2018 03 02	2	75 - 76	18	J. Horbowicz, K. Żukowski	Borowiec, Poland
2019 01 19 - 2019 03 30	3	151 - 162	5 - 13	V. Kudak, V. Perig	Derenivka, Ukraine
2019 03 23	1	152	10		Suhora, Poland
2019 04 01	1	151	12	E. Pakštienė	Moletai, Lithuania
(202) Chryseis					
2011 01 19 - 2011 04 01	15	140 - 151	1 - 16	Stephens et al. (2011)	GMARS, USA; Organ Mesa, USA; Hamanowa, Japan; Bigmuskie, Italy
2013 07 31	1	311	1	-	Montsec, Spain
2014 09 05	1	24	12	P. Kankiewicz	Kielce, Poland
2014 09 16 - 2014 10 05	2	19 - 23	4 - 9	A. Marciniak	Borowiec, Poland
2014 10 10 - 2014 10 26	2	15 - 18	3 - 6	G. Stachowski, W. Ogłoza	Suhora, Poland
2014 10 31 - 2014 11 20	3	12 - 14	8 - 13	-	Montsec, Spain
2014 11 03	1	14	9	S. Urakawa	Bisei, Japan
2015 10 27 - 2016 01 28	6	102 - 112	9 - 20	R. Hirsch, I. Konstanciak, A. Marciniak, P. Kulczak	Borowiec, Poland
2015 11 08	1	112	19	P. Kankiewicz	Kielce, Poland
2016 01 10 - 2016 02 23	3	100 - 106	3 - 17	F. Pilcher	Organ Mesa, USA
2017 03 20 - 2017 05 28	6	202 - 213	4 - 14	F. Pilcher	Organ Mesa, USA
2017 03 24 - 2017 04 18	3	208 - 212	4 - 10	-	Montsec, Spain
2017 03 24	1	212	10	V. Kudak, V. Perig	Derenivka, Ukraine
2017 03 27	1	212	9	A. Marciniak	Borowiec, Poland
2018 07 19 - 2018 09 13	10	280 - 284	4 - 16	-	Montsec, Spain
2019 08 23 - 2019 09 18	5	350 - 355	3 - 7	S. Fauvaud	Bardon, France
2019 08 25 - 2019 10 14	3	346 - 355	4 - 10	W. Ogłoza	Adiyaman, Turkey
2019 09 18 - 2019 09 20	3	350	3	-	Montsec, Spain
2019 10 05	1	347	7	K. Kamiński	Winer, USA
2019 10 07	1	346	8	V. Kudak, V. Perig	Derenivka, Ukraine
2019 10 14	1	346	10	R. Szakáts	Piszkéstető, Hungary
(219) Thusnelda					
1981 08 21 - 1981 09 27	7	340 - 347	8 - 14	Harris et al. (1992)	Table Mountain, USA
1981 09 02 - 1981 09 06	5	344 - 345	8 - 9	Lagerkvist & Kamel (1982)	ESO, Chile
2013 05 25 - 2013 06 30	14	236 - 238	6 - 21	-	Montsec, Spain
2013 05 27 - 2013 06 26	4	236 - 238	7 - 19	F. Pilcher	Organ Mesa, USA
2014 10 10 - 2014 12 24	26	81 - 95	7 - 26	Marciniak et al. (2015)	Suhora, Poland; Borowiec, Poland, Organ Mesa, USA; Winer, USA; Montsec, Spain; Bisei, Japan
2015 01 07	1	81	12	F. Pilcher	Organ Mesa, USA
2016 02 04 - 2016 03 06	5	181 - 186	5 - 15	-	Montsec, Spain
2016 02 08 - 2016 02 27	4	183 - 186	9 - 14	K. Kamiński	Winer, USA
2016 02 27 - 2016 03 31	4	175 - 183	2 - 9	F. Pilcher	Organ Mesa, USA
2016 04 02 - 2016 04 21	3	174 - 171	7 - 14	P. Kulczak, K. Żukowski, R. Hirsch	Borowiec, Poland
2017 05 26 - 2016 05 27	2	311	27	M.-Y. Kim	SOAO, South Korea
2017 06 23	1	314	22	R. Szakáts	Piszkéstető, Hungary
2017 07 03 - 2017 07 04	2	314	18 - 19	R. Duffard	La Sagra, Spain
2017 07 13 - 2017 08 16	4	306 - 313	12 - 15	S. Brincat	Flarestar, Malta
2017 07 13 - 2017 09 08	10	304 - 313	15 - 23	-	Montsec, Spain
2018 11 15 - 2019 02 08	2	125 - 135	8 - 22	V. Kudak, V. Perig	Derenivka, Ukraine
2018 12 10 - 2019 02 14	14	124 - 137	7 - 18	-	Montsec, Spain
2019 01 04 - 2019 01 31	6	127 - 134	6 - 12	F. Pilcher	Organ Mesa, USA
2019 01 30 - 2019 02 06	2	126 - 127	6 - 7	A. Marciniak	Borowiec, Poland
(223) Rosa					
2007 03 25 - 2007 04 14	4	166 - 169	5 - 12	Warner (2007b)	CSSS, USA
2011 12 30 - 2012 02 10	8	121 - 129	2 - 10	Pilcher (2012)	Organ Mesa, USA
2015 09 07 - 2015 10 09	3	344 - 350	1 - 10	S. Fauvaid	Le Bois de Bardon, France
2015 09 01 - 2015 09 03	2	347	4	S. Fauvaud, M. Fauvaud, F. Richard	
2015 11 22	1	344	18	D. Oszkiewicz	Lowell, USA
2016 11 01 - 2016 12 18	6	72 - 82	1 - 14	-	Montsec, Spain
2016 12 28	1	72	9	J. Horbowicz	Borowiec, Poland
2018 02 16 - 2018 02 25	2	184 - 185	9 - 12	R. Hirsch	Borowiec, Poland
2018 03 23	1	179	2	V. Kudak	Derenivka, Ukraine
2018 04 12 - 2018 04 19	8	174 - 175	9 - 11	-	Kepler Space Observatory
2019 05 15 - 2019 06 01	5	257 - 250	2 - 7	-	Montsec, Spain
2019 05 23	1	259	5	K. Kamiński	Winer, USA
2019 07 11	1	250	13	M. Ferrais	TRAPPIST-South, Chile
2020 07 19 - 2020 10 19	9	312 - 322	1 - 16	M. Ferrais	TRAPPIST-North, Morocco
2020 08 23 - 2020 08 25	4	316	4 - 5	F. Monteiro	OASI, Itacuruba, Brasil
2020 10 18 - 2020 10 19	2	313	16	M. Ferrais	TRAPPIST-South, Chile

Date	N_{lc}	λ [deg]	Phase angle [deg]	Observer	Site
(362) Havnia					
1978 12 04	1	63	5	Harris & Young (1980)	Table Mountain, USA
2006 06 05 - 2006 08 26	5	299 - 312	9 - 19	-	SuperWASP
2009 04 06 - 2009 04 20	6	180 - 186	5 - 11	Stephens (2009)	Rancho Cucamonga, USA
2015 10 28 - 2015 12 10	3	24 - 30	2 - 19	M. Butkiewicz - Bąk, A. Marciniak, P. Kulczak	Borowiec, Poland
2015 11 29 - 2015 12 01	2	24	16	-	Montsec, Spain
2016 12 22 - 2017 03 03	4	152 - 160	6 - 21	J. Horbowicz, A. Marciniak, K. Żukowski, M. Butkiewicz - Bąk	Borowiec, Poland
2017 01 19	1	161	15	V. Kudak, V. Perig	Derenivka, Ukraine
2017 01 25 - 2017 01 31	7	159 - 160	11 - 13	T. Polakis, B. Skiff	Command Module, USA
2018 07 26	1	252	17	A. Marciniak	CTIO, Chile
2019 08 29 - 2019 09 19	2	17 - 20	8 - 16	S. Fauvaud	Bardon, France
2019 09 04	1	19	14	V. Kudak, V. Perig	Derenivka, Ukraine
2019 09 21	1	16	7	J. Skrzypek	Borowiec, Poland
2019 09 28 - 2019 10 15	2	11 - 15	4 - 5	W. Ogłoza	Adiyaman, Turkey
2019 10 17 - 2020 01 10	2	10 - 14	6 - 13	R. Szakáts	Piszkéstető, Hungary
(483) Seppina					
1986 07 11 - 1986 07 27	6	268 - 270	9 - 12	Zappalà et al. (1989)	ESO, La Silla, Chile
2005 06 25 - 2005 07 11	2	264 - 266	8 - 10	F. Manzini	Sozzago, Italy
2005 07 04	1	265	9	G. Farroni, P. Pinel	Saint-Avertin, France
2005 07 10 - 2005 07 30	4	262 - 264	10 - 13	R. Roy	Blauvac, France
2005 07 12	1	264	11	L. Bernasconi	Engarouines, France
2006 08 21	1	348	6	L. Brunetto	Le Florian, France
2013 10 08 - 2013 12 23	4	25 - 34	5 - 16	K. Sobkowiak, D. Oszkiewicz, A. Marciniak	Borowiec, Poland
2013 12 16 - 2013 12 17	4	25 - 33	5 - 15	F. Pilcher	Organ Mesa, USA
2015 01 20 - 2015 03 22	3	96 - 97	9 - 16	K. Kamiński	Winer, USA
2015 02 12 - 2015 03 18	2	94 - 95	13 - 16	A. Marciniak, J. Horbowicz, M. Figas	Borowiec, Poland
2016 01 03 - 2016 04 01	5	155 - 167	5 - 14	P. Kulczak, A. Marciniak, R. Hirsch, M. Butkiewicz - Bąk	Borowiec, Poland
2017 04 01 - 2017 05 29	9	214 - 224	5 - 10	R. Hirsch, K. Żukowski, J. Horbowicz, A. Marciniak, J. Skrzypek	Borowiec, Poland
2018 07 19 - 2018 08 15	14	287 - 291	7 - 12	-	Montsec, Spain
(501) Urhixidur					
1990 08 22 - 1990 08 29	6	327 - 329	6 - 7	Lagerkvist et al. (1992)	ESO, La Silla, Chile
2013 09 06 - 2013 12 30	5	18 - 28	6 - 20	R. Hirsch, T. Santana-Ros, D. Oszkiewicz, A. Marciniak	Borowiec, Poland
2014 10 29 - 2015 03 17	6	104 - 117	8 - 18	R. Hirsch, A. Marciniak, I. Konstanciak, J. Horbowicz	Borowiec, Poland
2015 01 21 - 2015 04 29	2	109 - 111	8 - 16	K. Kamiński	Winer, USA
2015 03 22 - 2015 03 23	2	105	17	W. Ogłoza, A. Marciniak, V. Kudak	Suhora, Poland
2016 02 06 - 2016 04 29	4	163 - 176	2 - 14	A. Marciniak, R. Hirsch	Borowiec, Poland
2016 02 13 - 2016 03 01	4	172 - 175	3 - 8	K. Kamiński	Winer, USA
2017 02 08 - 2017 03 09	2	231 - 233	15 - 16	A. Marciniak	CTIO, Chile
2017 05 04	1	227	7	F. Monteiro	OASI, Brasil
2018 08 04 - 2018 08 22	18	312 - 315	8 - 9	Pál et al. (2020)	TESS Spacecraft
2018 08 14	1	313	8	A. Marciniak	CTIO, Chile
2018 09 14 - 2018 09 15	2	309	15	F. Monteiro	OASI, Brasil
2019 08 12 - 2019 08 19	4	58 - 59	21	W. Ogłoza	Adiyaman, Turkey
2019 10 11 - 2019 12 15	2	52 - 64	12 - 15	R. Szakáts, V. Kecskeméthy	Piszkéstető, Hungary
2019 10 12 - 2019 10 15	2	64	14 - 15	J. Skrzypek, M. Pawłowski	Borowiec, Poland
(537) Pauly					
1984 05 10	1	211	8	Weidenschilling et al. (1990)	Kitt Peak, USA
1985 09 08 - 1985 09 12	4	354 - 355	6	Barucci et al. (1992)	ESO, Chile
1989 04 16	1	182	7	Weidenschilling et al. (1990)	Kitt Peak, USA
2016 02 24 - 2016 03 10	4	202 - 204	10 - 13	K. Kamiński	Winer, USA
2016 03 18 - 2016 05 09	4	191 - 201	8 - 12	M. Butkiewicz - Bąk, A. Marciniak, P. Kulczak	Borowiec, Poland
2017 08 03 - 2017 09 24	9	311 - 316	2 - 19	-	Montsec, Spain
2018 10 09 - 2018 11 29	5	65 - 73	4 - 15	K. Żukowski, A. Marciniak, M. K. Kamińska, J. Krajewski, M. Pawłowski	Borowiec, Poland
2018 11 26 - 2018 12 10	16	62 - 66	4 - 6	Pál et al. (2020)	TESS Spacecraft
2019 11 24 - 2019 12 17	3	126 - 128	10 - 14	W. Ogłoza	Adiyaman, Turkey
2019 11 27	1	128	14	M.-Y. Kim, D.-H. Kim	SOAO, South Korea
2019 12 05	1	127	12	A. Marciniak	Borowiec, Poland
2020 01 15	1	122	2	V. Kudak, V. Perig	Derenivka, Ukraine
(552) Sigelinde					
2008 04 11 - 2008 05 03	8	245 - 247	7 - 14	Oey (2009)	Leura, Australia
2010 08 13 - 2011 01 26	11	42 - 52	2 - 18	Waszczak et al. (2015)	Palomar Transient Factory, USA
2015 08 25 - 2015 10 02	5	6 - 12	3 - 12	A. Marciniak, R. Hirsch, P. Kulczak	Borowiec, Poland
2016 11 20 - 2016 12 05	2	74 - 76	1 - 5	K. Żukowski, R. Hirsch	Borowiec, Poland
2017 01 15	1	67	12	S. Geier	ORM, Spain
2017 01 25	1	67	14	M.-Y. Kim, D.-H. Kim	SOAO, South Korea
2017 02 08	1	67	16	A. Marciniak	CTIO, Chile
2017 02 10 - 2017 02 11	2	67	16	M.-Y. Kim, D.-H. Kim	BOAO, South Korea
2018 02 23 - 2018 04 09	3	132 - 136	6 - 17	A. Marciniak, R. Hirsch, K. Żukowski	Borowiec, Poland
2018 03 14 - 2018 03 16	2	133	12	M.-Y. Kim, D.-H. Kim	BOAO, South Korea
2018 03 19	1	133	13	K. Kamiński	Winer, USA
2019 04 26 - 2019 04 29	4	224 - 225	3 - 4	K. Kamiński	Winer, USA
2019 05 11	1	222	4	-	Montsec, Spain
2019 04 26 - 2019 05 19	23	220 - 225	3 - 7	Pál et al. (2020)	TESS Spacecraft

Date	N_{lc}	λ [deg]	Phase angle [deg]	Observer	Site
(618) Elfriede					
1984 05 12	1	236	6	Weidenschilling et al. (1990)	Kitt Peak, USA
1989 04 16 - 1989 04 17	2	183	9	Weidenschilling et al. (1990)	Kitt Peak, USA
2004 12 03 - 2004 12 11	6	125	12 - 14	L. Bernasconi	Engarouines, France
2006 05 12 - 2006 06 02	7	175 - 176	15 - 17	Warner (2006)	Palmer Divide, USA
2014 10 01 - 2014 12 09	12	4 - 10	8 - 18	-	Montsec, Spain
2015 10 10 - 2016 01 27	5	86 - 98	4 - 18	-	Montsec, Spain
2016 01 22	1	87	10	A. Marciniak	Borowiec, Poland
2016 12 29 - 2017 04 09	4	150 - 163	8 - 15	J. Horbowicz, K. Żukowski	Borowiec, Poland
2017 01 25	1	162	10	M.-Y. Kim, D.-H. Kim	SOAO, South Korea
2017 02 04 - 2017 03 14	2	153 - 160	8		Suhora, Poland
2017 02 22 - 2017 02 25	4	157	5	T. Polakis, B. Skiff	Command Module, USA
2017 03 02 - 2017 03 17	9	153 - 156	5 - 8	Klinglesmith et al. (2017)	Socorro, USA
2018 02 27 - 2018 05 09	5	226 - 232	7 - 17	K. Żukowski, J. Horbowicz, A. Marciniak, J. Skrzypek	Borowiec, Poland
2019 07 22 - 2019 07 26	5	306	2 - 3	W. Ogłoza	Adiyaman, Turkey
(666) Desdemona					
2013 10 02 - 2014 02 14	8	82 - 95	9 - 29	Marciniak et al. (2015)	Borowiec, Poland; Winer, USA
2014 12 31 - 2015 03 14	15	192 - 196	5 - 19	-	Montsec, Spain
2015 02 11 - 2015 03 31	2	186 - 197	6 - 15	K. Kamiński	Winer, USA
2015 03 18	1	191	5	M. Figas	Borowiec, Poland
2016 04 16	2	264	16	S. Geier	Kitt Peak, USA
2016 04 29	1	264	13	S. Geier	ORM, Spain
2016 05 01	1	263	13	-	Montsec, Spain
2016 06 30 - 2016 07 05	4	251 - 252	10 - 11	R. Duffard, N. Morales	La Sagra, Spain
2016 07 23	1	249	17	A. Marciniak	Teide, Spain
2017 09 16 - 2017 09 22	7	57 - 58	27 - 25	T. Polakis, B. Skiff	Tempe, USA
2017 09 18 - 2018 01 08	5	48 - 58	5 - 25	J. Horbowicz, K. Żukowski, R. Hirsch	Borowiec, Poland
2019 01 07	1	184	19	R. Duffard, N. Morales	La Sagra, Spain
2019 02 01 - 2019 04 07	6	172 - 184	3 - 15	-	Montsec, Spain
2019 02 07	1	184	14	Cs. Kalup	Piszkéstető, Hungary
2019 04 01 - 2019 04 03	2	173	6 - 7	M. Pawłowski, J. Krajewski	Borowiec, Poland
(667) Denise					
2014 03 28 - 2014 05 19	5	166 - 169	8 - 19	R. Hirsch, K. Sobkowiak, I. Konstanciak, P. Trela	Borowiec, Poland
2015 03 23 - 2015 03 24	2	252	15	W. Ogłoza, A. Marciniak. V. Kudak	Suhora, Poland
2015 04 21 - 2015 04 23	2	250 - 251	12	J. Horbowicz, A. Marciniak	Borowiec, Poland
2015 05 31	1	243	9	K. Kamiński	Winer, USA
2015 06 27	1	238	12	A. Marciniak	Teide, Spain
2016 07 23 - 2016 07 26	3	298	5 - 6	-	Montsec, Spain
2016 07 30 - 2016 08 20	4	293 - 297	6 - 10	R. Szakáts, E. Verebélyi	Piszkéstető, Hungary
2016 08 26	1	293	11	S. Geier	ORM, Spain
2016 08 31	1	292	12	K. Żukowski	Borowiec, Poland
2017 08 07	1	359	12		Suhora, Poland
2017 08 27	1	357	8	A. Marciniak	Teide, Spain
2017 08 31 - 2017 09 18	8	352 - 356	4 - 6	-	Montsec, Spain
2018 11 23 - 2019 01 27	9	96 - 108	15 - 18	-	Montsec, Spain
2019 02 18	1	94	19	M. K. Kamińska	Borowiec, Poland
(780) Armenia					
2004 06 07 - 2004 07 15	3	256 - 263	8 - 13	J.-G. Bosch	Collonges, France
2009 05 02 - 2009 06 02	15	217 - 223	8 - 12	Benishek & Pilcher (2009)	Organ Mesa, USA; Belgrade, Serbia
2010 07 20 - 2010 08 31	2	298 - 306	5 - 13	R. Roy	Blauvac, France
2014 02 25 - 2014 05 31	8	182 - 194	11 - 15	J. Horbowicz, A. Marciniak, I. Konstanciak, D. Oszkiewicz, T. Santana - Ros, K. Sobkowiak	Borowiec, Poland
2015 04 16 - 2015 05 30	4	265 - 268	9 - 16	P. Kulczak, A. Marciniak	Borowiec, Poland
2015 05 21 - 2015 06 22	7	260 - 266	8 - 11	K. Kamiński	Winer, USA
2015 06 17 - 2015 07 06	11	257 - 261	8 - 11	-	Montsec, Spain
2016 08 02	1	355	8	A. Marciniak	CTIO, Chile
2016 10 08 - 2016 10 15	2	346	11 - 13	-	Montsec, Spain
2016 10 10 - 2016 11 08	12	345 - 346	11 - 18	B. Skiff	Lowell, USA
2016 12 04 - 2016 12 05	2	348	20	T. Polakis, B. Skiff	Command Module, USA
2017 12 15 - 2017 01 21	3	84 - 91	8 - 12	F. Monteiro	OASI, Brasil
2017 12 17 - 2018 02 13	3	83 - 90	7 - 16	M.-Y. Kim, D.-H. Kim	SOAO, South Korea
2018 01 03 - 2018 01 05	2	86 - 87	8 - 9	M.-Y. Kim, D.-H. Kim	Mt Lemmon, USA
2018 01 24 - 2018 03 27	2	84 - 88	13 - 18	K. Kamiński	Winer, USA
2018 02 08 - 2018 02 16	2	83	16 - 17	M. Butkiewicz - Bąk, R. Hirsch	Borowiec, Poland
2018 12 04 - 2019 01 06	3	163 - 165	14 - 17	M.-J. Kim, D-H. Kim	SOAO, South Korea
2019 01 19 - 2019 03 30	6	152 - 164	2 - 12	R. Hirsch, J. Krajewski, A. Marciniak, K. Żukowski, J. Skrzypek	Borowiec, Poland
2019 02 22	1	159	2	V. Kudak, V. Perig	Derenivka, Ukraine
(923) Herluga					
2008 10 07 - 2008 11 29	8	39 - 49	8 - 16	Brinsfield (2009)	Via Capote, USA
2012 10 19 - 2012 10 31	2	354 - 355	14 - 19	R. Hirsch, J. Nadolny	Borowiec, Poland
2014 03 14 - 2014 04 18	7	149 - 152	9 - 18	-	Montsec, Spain
2015 03 17 - 2015 03 27	6	227 - 238	7 - 16	-	Montsec, Spain
2015 04 18 - 2015 06 22	3	223 - 235	4 - 14	K. Kamiński	Winer, USA
2016 07 25 - 2016 09 10	12	330 - 320	8 - 14	Marciniak et al. (2018)	Montsec, Spain; ORM, Spain; Borowiec, Poland
2018 03 18 - 2018 03 30	3	126	18 - 20	K. Kamiński	Winer, USA
2019 03 30 - 2019 04 01	3	220	9 - 10	R. Szakáts	Piszkéstető, Hungary
2019 04 26 - 2019 05 11	7	211 - 215	2 - 7	-	Montsec, Spain

Date	N_{lc}	λ [deg]	Phase angle [deg]	Observer	Site
(995) Sternberga					
1989 01 07 - 1989 01 12	4	124 - 126	8 - 9	Barucci et al. (1992)	ESO, La Silla, Chile
2007 03 21 - 2007 03 24	2	211 - 212	9 - 10	-	Super WASP
2012 06 30 - 2012 07 15	10	292 - 292	9 - 11	Stephens (2013)	Racho Cucamonga, USA
2013 11 13 - 2014 02 04	4	79 - 93	7 - 18	A. Marciniak, I. Konstanciak, P. Trela, J. Horbowicz, R. Hirsch	Borowiec, Poland
2013 12 06 - 2013 12 15	5	87 - 89	5 - 7	F. Pilcher	Organ Mesa, USA
2014 01 02 - 2014 02 21	4	80 - 82	9 - 20	K. Kamiński	Winer, USA
2015 01 01 - 2015 03 16	15	169 - 178	5 - 18	-	Montsec, Spain
2015 02 11	1	177	11	K. Kamiński	Winer, USA
2015 02 25	1	174	7	F. Pilcher	Organ Mesa, USA
2015 03 23	1	168	7	R. Hirsch	Borowiec, Poland
2016 05 04 - 2016 07 10	24	252 - 265	5 - 15	Marciniak et al. (2018)	Lowell, USA; Teide, Spain; Derenivka, Ukraine; Command Module, USA; La Sagra, Spain; Montsec, Spain; Bardon, France
2017 10 24	1	66	14	V. Kudak, V. Perig	Derenivka, Ukraine
2017 12 07 - 2018 02 06	3	53 - 56	8 - 22	M. Butkiewicz - Bąk, R. Hirsch, J. Skrzypek	Borowiec, Poland

(362) Havnia, 2017-01-07	
P. Maley	Gila Bend, AZ
C. Wiesenborn	Boulder City, NV
W. Thomas	Florence, AZ
T. George	Scottsdale, AZ
(618) Elfriede, 2008-05-26	
D. Breadsell	Toowoomba, Qld, AU
J. Bradshaw	Samford, Qld, AU
P. Anderson	Range Observatory, Qld, AU
(618) Elfriede, 2013-04-13	
D. Herald	Murrumbateman, NSW
J. Drummond	Patutahi, Gisborne, NZ
(618) Elfriede, 2015-12-30	
J. Rovira	ES
R. Naves	ES
C. Perello, A. Selva	ES
C. Schnabel	ES
(618) Elfriede, 2018-05-10	
J. Broughton	Woodburn, NSW, AU
J. Broughton	Grafton, NSW, AU
J. Broughton	Mullaway, NSW, AU
(667) Denise, 2008-04-08	
R. Nugent	Pontotoc, TX
G. Nason	Tobermory, ONT, CA
M. McCants	Kingsland, TX
P. Maley, D. Weber	Horseshoe Bay, TX
(667) Denise, 2020-04-11	
S. Meister	CH
A. Schweizer	CH
C. Ellington	DE
S. Sposetti	CH
A. Manna	CH
A. Ossola	CH
O. Schreurs	BE
M. Bigi	IT
P. Baruffetti	IT
F. Van Den Abbeel	BE
J. Bourgeois	BE
R. Boninsegna	BE
(667) Denise, 2020-05-10	
K. Hanna	MT
K. Green	CT
R. Kamin	PA
S. Conard	MD
K. Getrost	OH
A. Scheck	MD
A. Caroglanian	MD
J. Massura	IN
J. Harris	VA
C. Anderson, K. Thomason	ID
M. Wasiuta, B. Billard	VA
B. Billard	VA

Table 5: List of stellar occultation observers and locations of the observing sites.

[1] Astronomical Observatory Institute, Faculty of Physics, A. Mickiewicz University, Słoneczna 36, 60-286 Poznań, Poland. E-mail: am@amu.edu.pl
[2] Astronomical Institute, Faculty of Mathematics and Physics, Charles University, V Holešovičkách 2, 180 00 Prague 8, Czech Republic
[3] Max-Planck-Institut für Extraterrestrische Physik, Giessenbachstrasse 1, 85748 Garching, Germany
[4] Mt. Suhora Observatory, Pedagogical University, Podchorążych 2, 30-084, Cracow, Poland
[5] Konkoly Observatory, Research Centre for Astronomy and Earth Sciences, Hungarian Academy of Sciences, H-1121 Budapest, Konkoly Thege Miklós út 15-17, Hungary
[6] MTA CSFK Lendület Near-Field Cosmology Research Group
[7] Astronomy Department, Eötvös Loránd University, Pázmány P. s. 1/A, H-1171 Budapest, Hungary
[8] Geneva Observatory, CH-1290 Sauverny, Switzerland
[9] Les Engarouines Observatory, F-84570 Mallemort-du-Comtat, France
[10] Collonges Observatory, F-74160 Collonges, France
[11] Flarestar observatory, Malta
[12] "Le Florian", Villa 4, F-06600 Antibes, France
[13] Haute-Provence Observatory, St-Michel l'Observatoire, France
[14] Departamento de Sistema Solar, Instituto de Astrofísica de Andalucía (CSIC), Glorieta de la Astronomía s/n, 18008 Granada, Spain
[15] 11 rue du Puits Coellier, F-37550 Saint-Avertin, France
[16] Observatoíre du Bois de Bardon, 16110 Taponnat, France
[17] Aix Marseille Université, CNRS, CNES, Laboratoire d'Astrophysique de Marseille, Marseille, France
[18] Instituto de Astrofísica de Canarias, C/ Vía Lactea, s/n, 38205 La Laguna, Tenerife, Spain
[19] Gran Telescopio Canarias (GRANTECAN), Cuesta de San José s/n, E-38712, Breña Baja, La Palma, Spain
[20] Faculty of Physics, Astronomy and Informatics, Nicolaus Copernicus University in Toruń
[21] School of Physical Sciences, The Open University, MK7 6AA, UK
[22] Space sciences, Technologies and Astrophysics Research Institute, Université de Liège, Allée du 6 Août 17, 4000 Liège, Belgium
[23] Astrophysics Division, Institute of Physics, Jan Kochanowski University, Świetokrzyska 15, 25-406 Kielce, Poland
[24] Chungbuk National University, 1, Chungdae-ro, Seowon-gu, Cheongju-si, Chungcheongbuk-do, Republic of Korea
[25] Korea Astronomy and Space Science Institute, 776 Daedeokdae-ro, Yuseong-gu, 305-348 Daejeon, Korea
[26] Institute of Physics, Faculty of Natural Sciences, University of P. J. Šafárik, Park Angelinum 9, 040 01 Košice, Slovakia
[27] Laboratory of Space Researches, Uzhhorod National University, Daleka st. 2a, 88000, Uzhhorod, Ukraine
[28] Observatório Nacional Rua General José Cristino, 77, 20921-400 Bairro Imperial de São Cristóvão Rio de Janeiro, RJ, Brasil
[29] Universidad de La Laguna, Dept. Astrofisica, E.38206 La Laguna, Tenerife, Spain
[30] Institute of Theoretical Physics and Astronomy, Vilnius University, Saulėtekio al. 3, 10257 Vilnius, Lithuania
[31] 4438 Organ Mesa Loop, Las Cruces, New Mexico 88011 USA
[32] Command Module Observatory, 121 W. Alameda Dr., Tempe, AZ 85282 USA
[33] Observatoire de Blauvac, 293 chemin de St Guillaume, F-84570 St-Estève, France
[34] Departamento de Física, Ingeniería de Sistemas y Teoría de la Señal, Universidad de Alicante, Alicante, Spain
[35] Institut de Ciències del Cosmos, Universitat de Barcelona (IEEC-UB), Barcelona, Spain
[36] Lowell Observatory, 1400 West Mars Hill Road, Flagstaff, Arizona, 86001 USA
[37] University of Adiyaman, Department of Physics, 02040 Adiyaman, Turkey
[38] Leiden Observatory, Leiden University, PO Box 9513, 2300 RA Leiden, The Netherlands
[39] Bisei Spaceguard Center, Japan Spaceguard Association, 1716-3, Okura, Bisei, Ibara, Okayama 714-1411, Japan
[40] Kepler Institute of Astronomy, University of Zielona Góra, Lubuska 2, 65-265 Zielona Góra, Poland

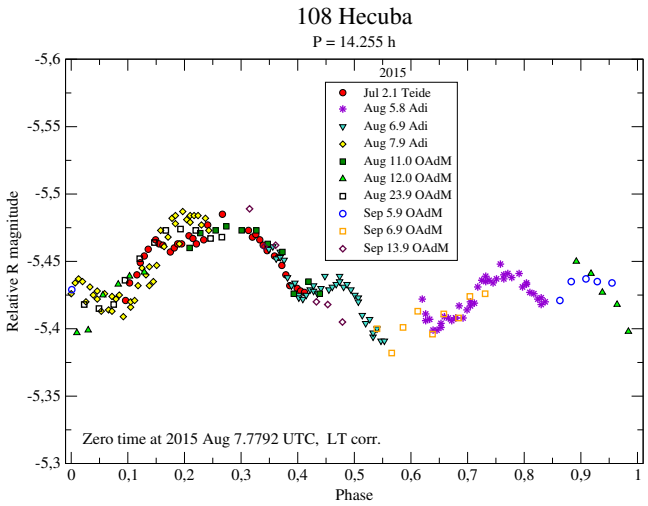

Fig. 45: Composite lightcurve of (108) Hecuba from the year 2015.

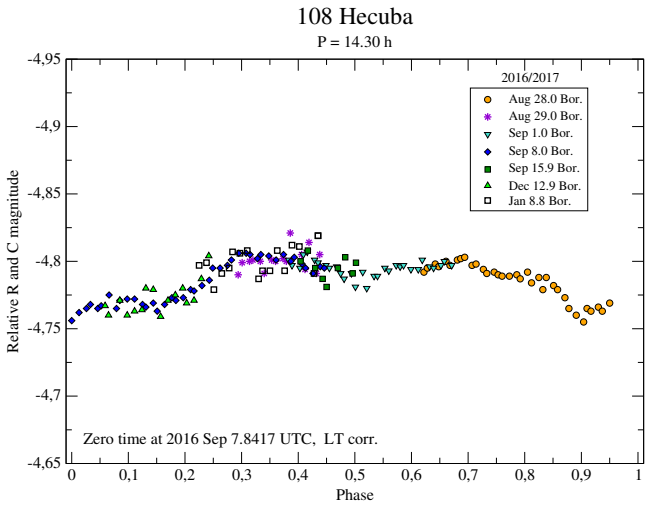

Fig. 46: Composite lightcurve of (108) Hecuba from the years 2016-2017.

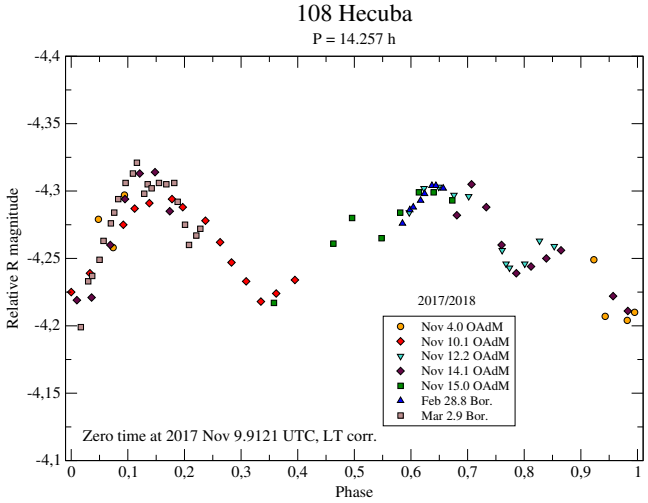

Fig. 47: Composite lightcurve of (108) Hecuba from the years 2017-2018.

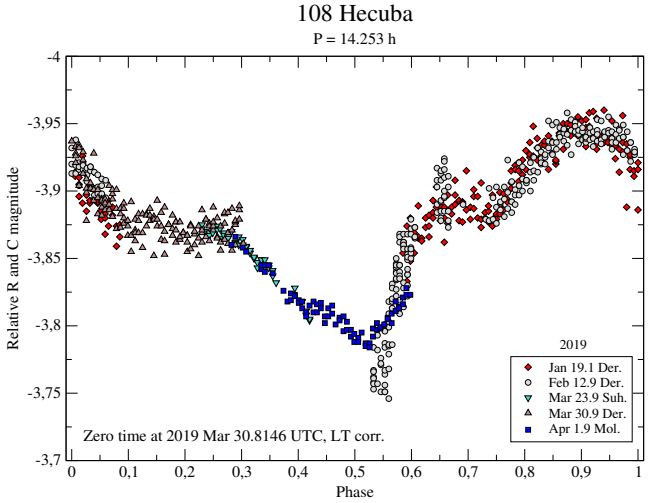

Fig. 48: Composite lightcurve of (108) Hecuba from the year 2019.

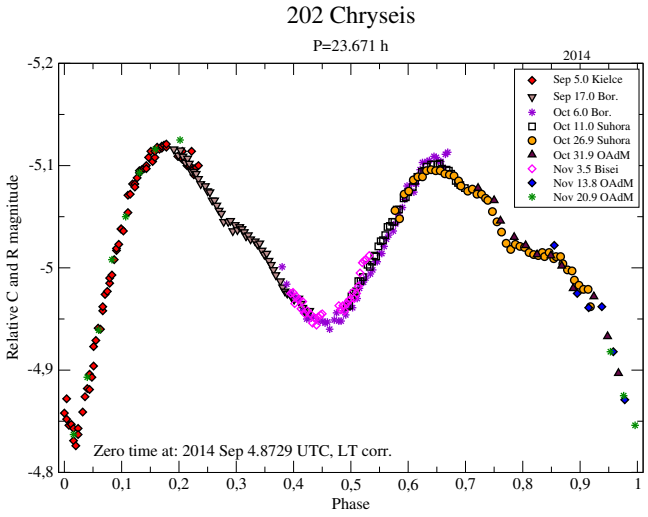

Fig. 49: Composite lightcurve of (202) Chryseis from the year 2014.

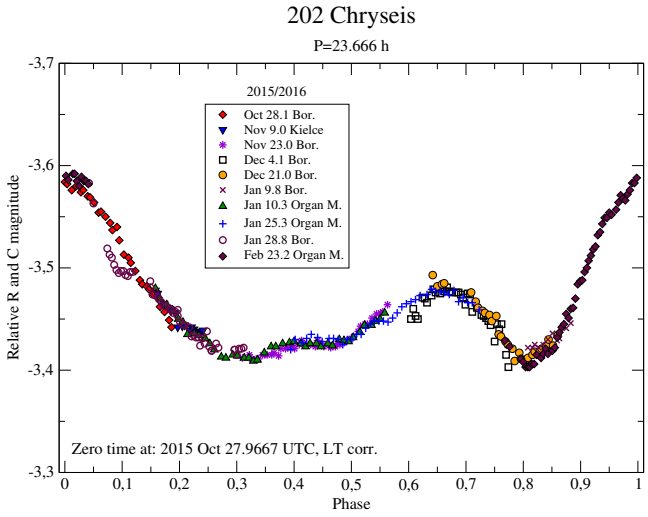

Fig. 50: Composite lightcurve of (202) Chryseis from the years 2015-2016.

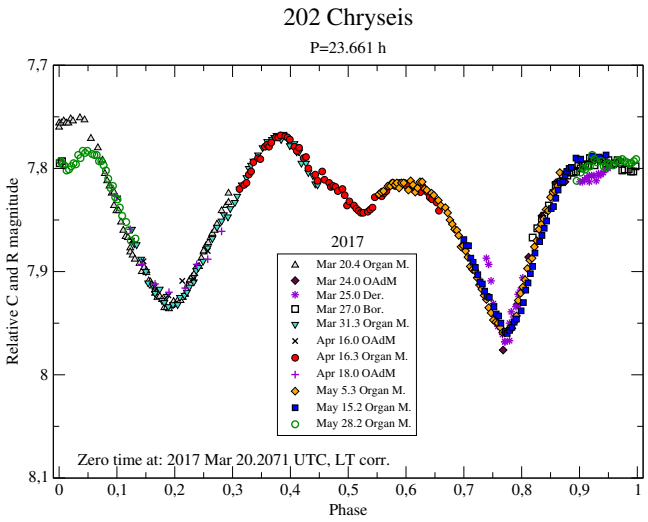

Fig. 51: Composite lightcurve of (202) Chryseis from the year 2017.

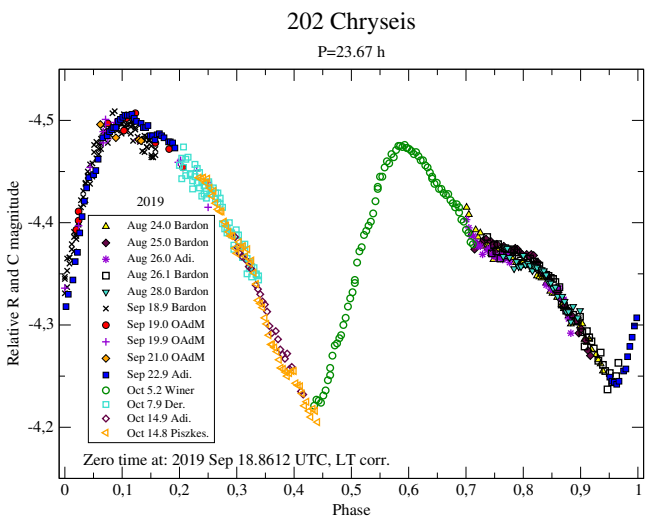

Fig. 52: Composite lightcurve of (202) Chryseis from the year 2019.

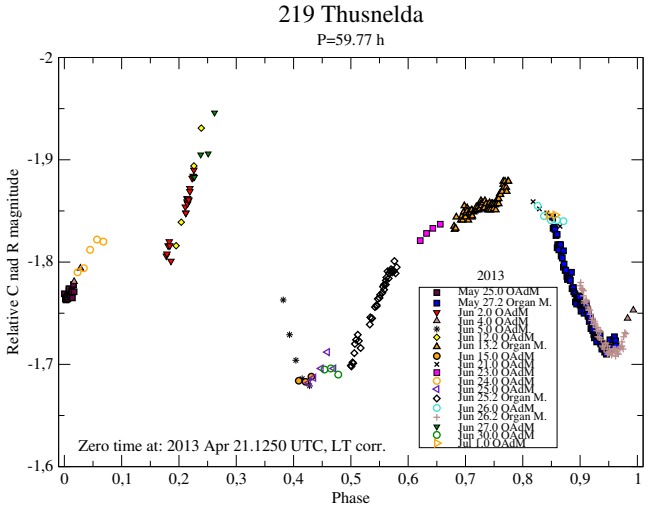

Fig. 53: Composite lightcurve of (219) Thusnelda from the year 2013.

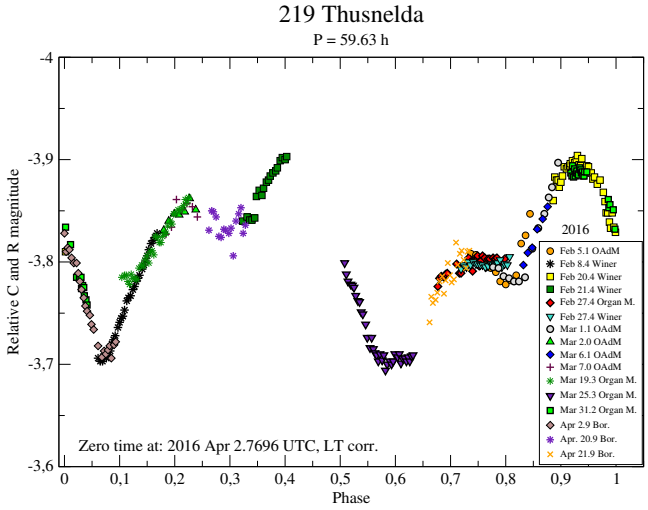

Fig. 54: Composite lightcurve of (219) Thusnelda from the year 2016.

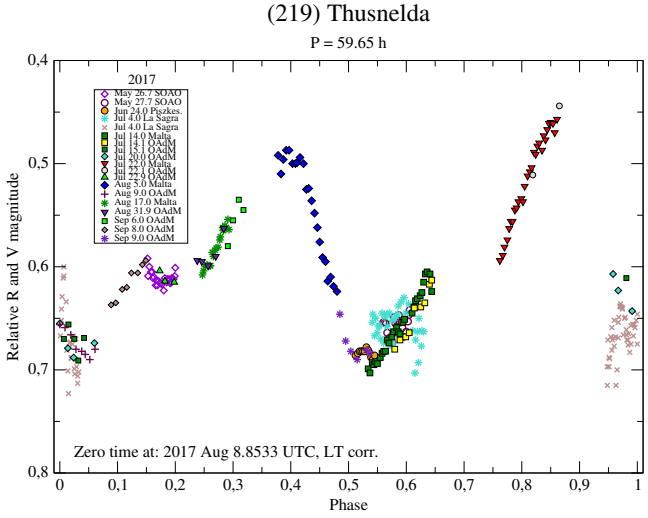

Fig. 55: Composite lightcurve of (219) Thusnelda from the year 2017.

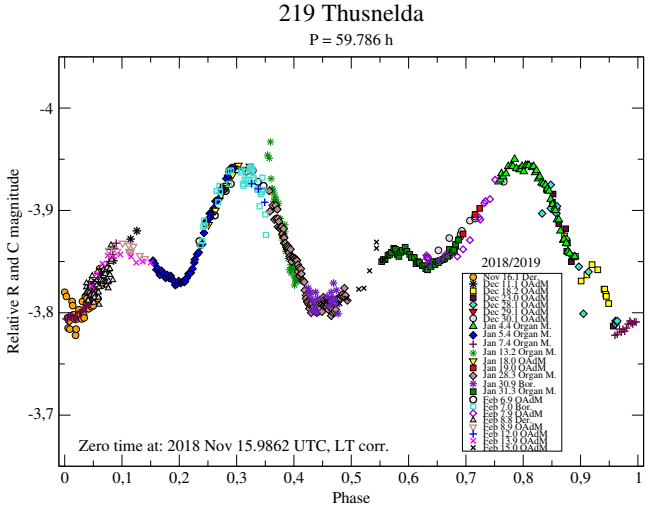

Fig. 56: Composite lightcurve of (219) Thusnelda from the years 2018-2019.

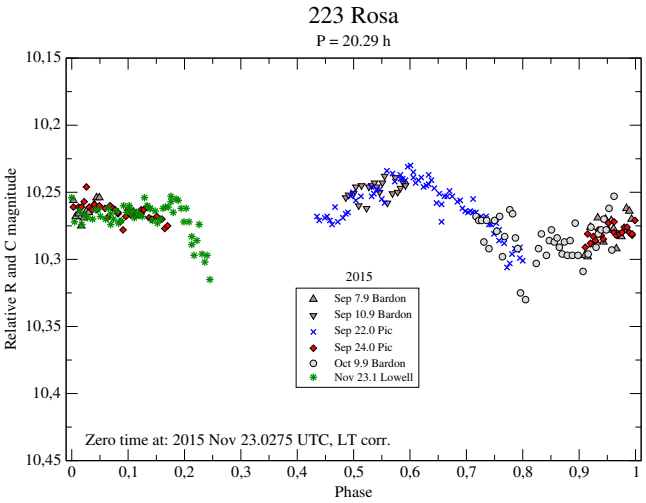

Fig. 57: Composite lightcurve of (223) Rosa from the year 2015.

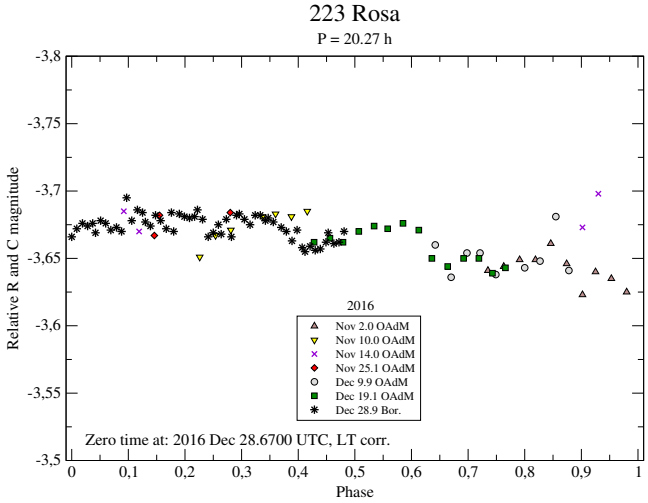

Fig. 58: Composite lightcurve of (223) Rosa from the year 2016.

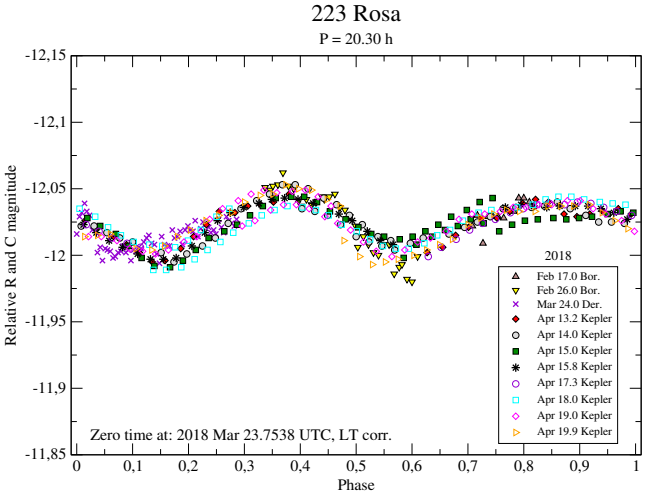

Fig. 59: Composite lightcurve of (223) Rosa from the year 2018.

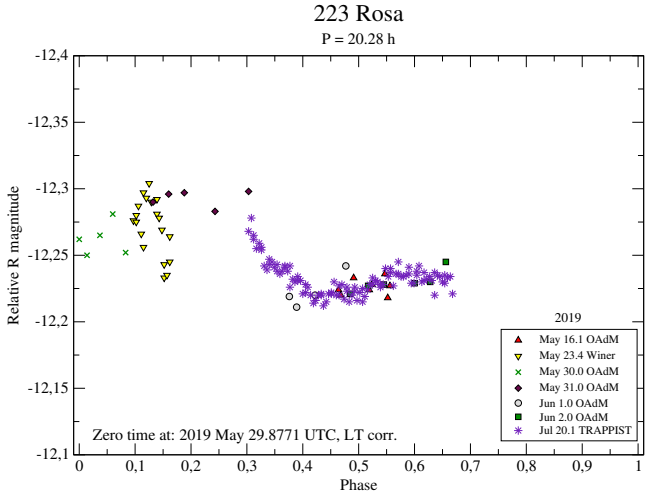

Fig. 60: Composite lightcurve of (223) Rosa from the year 2019.

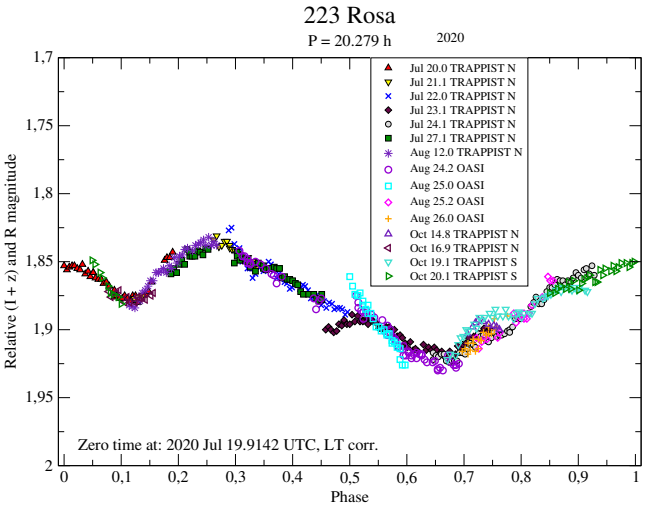

Fig. 61: Composite lightcurve of (223) Seppina from the year 2020.

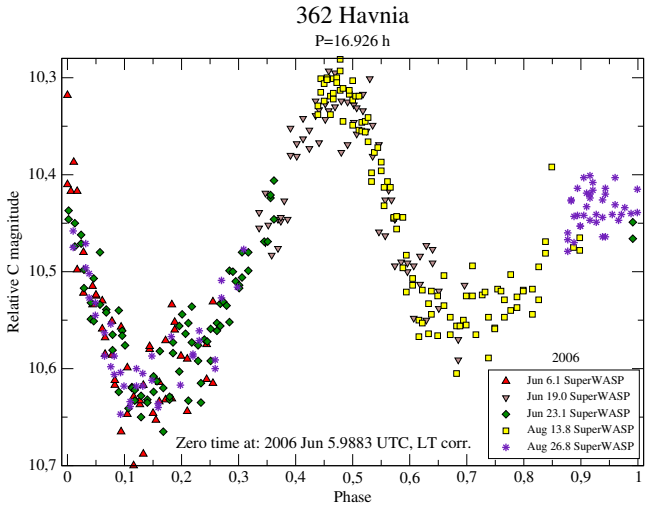

Fig. 62: Composite lightcurve of (362) Havnia from the year 2006.

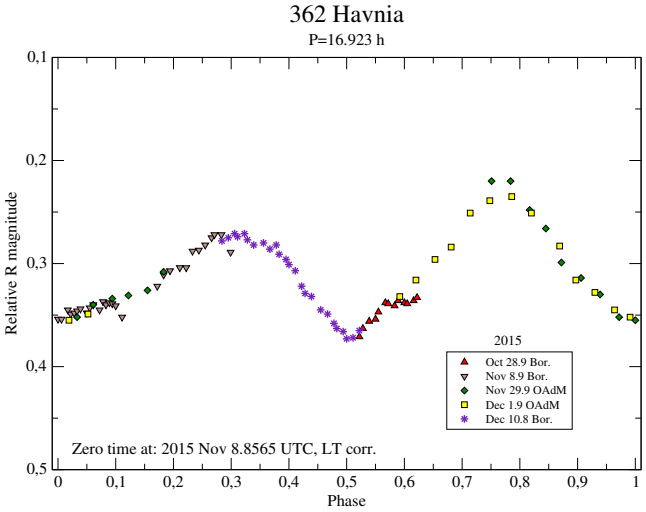

Fig. 63: Composite lightcurve of (362) Havnia from the year 2015.

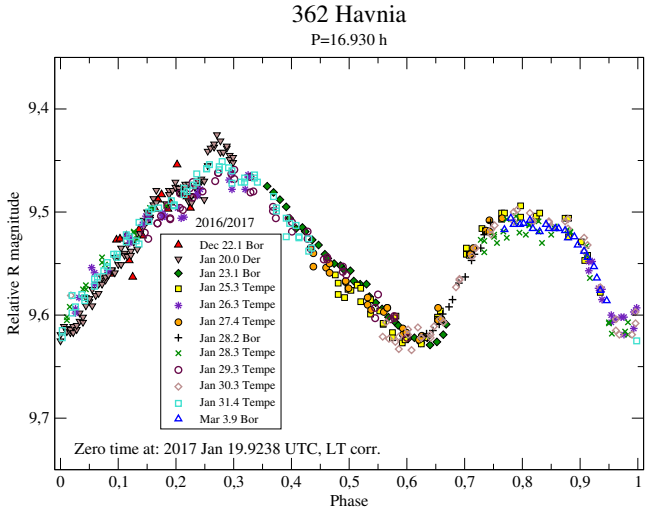

Fig. 64: Composite lightcurve of (362) Havnia from the years 2016-2017.

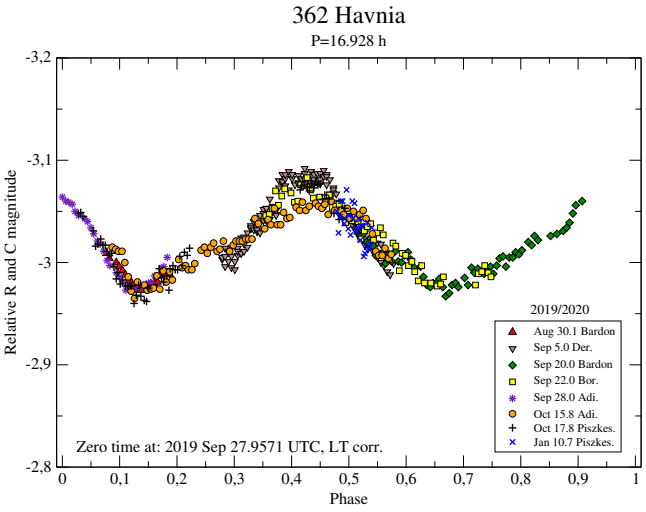

Fig. 65: Composite lightcurve of (362) Havnia from the years 2019 2020.

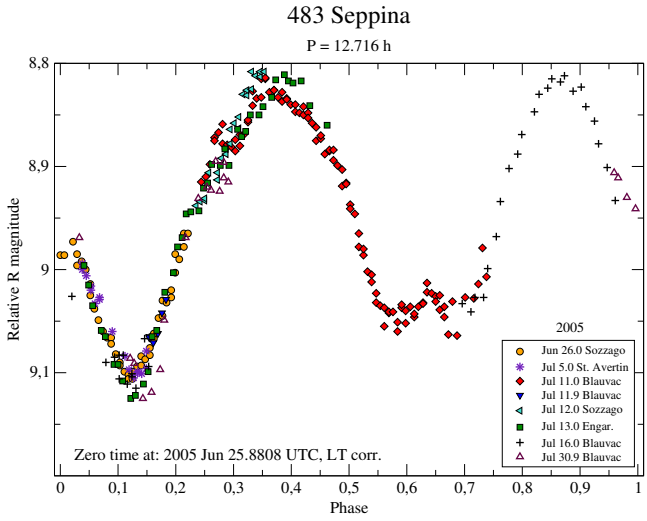

Fig. 66: Composite lightcurve of (483) Seppina from the year 2005.

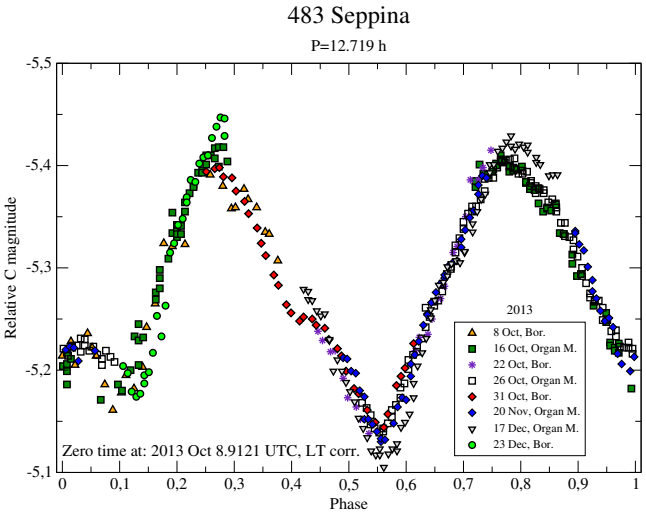

Fig. 67: Composite lightcurve of (483) Seppina from the year 2013.

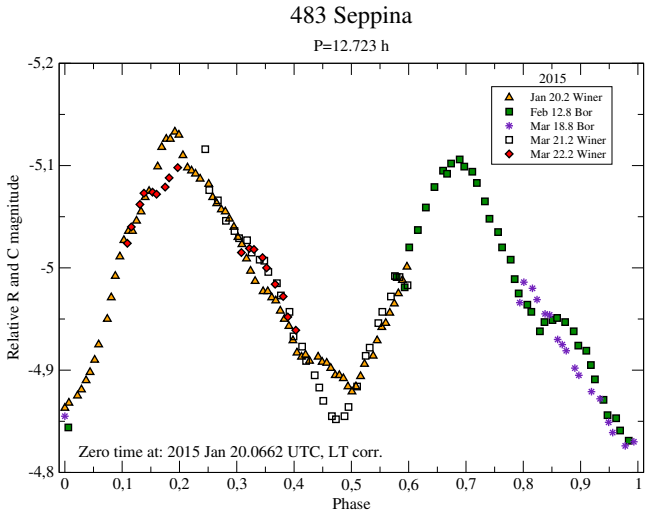

Fig. 68: Composite lightcurve of (483) Seppina from the year 2015.

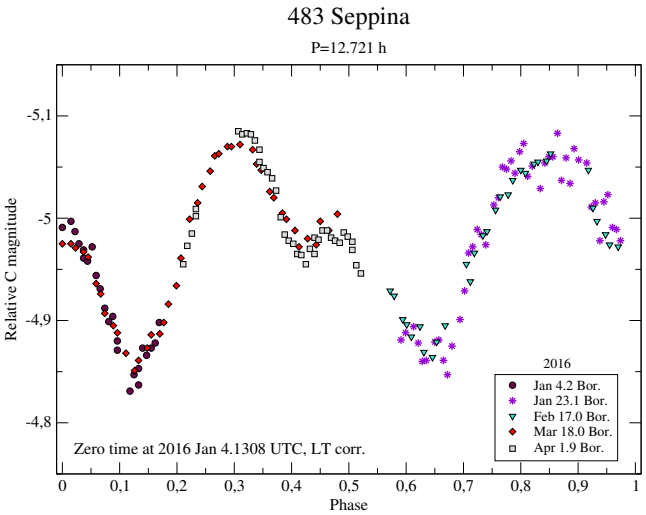

Fig. 69: Composite lightcurve of (483) Seppina from the year 2016.

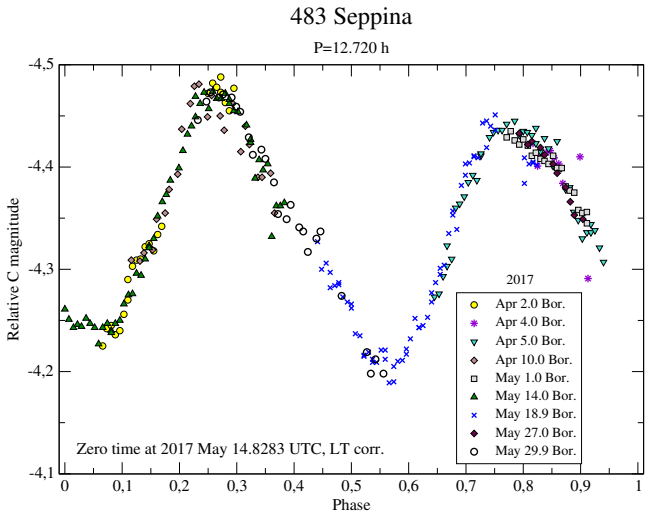

Fig. 70: Composite lightcurve of (483) Seppina from the year 2017.

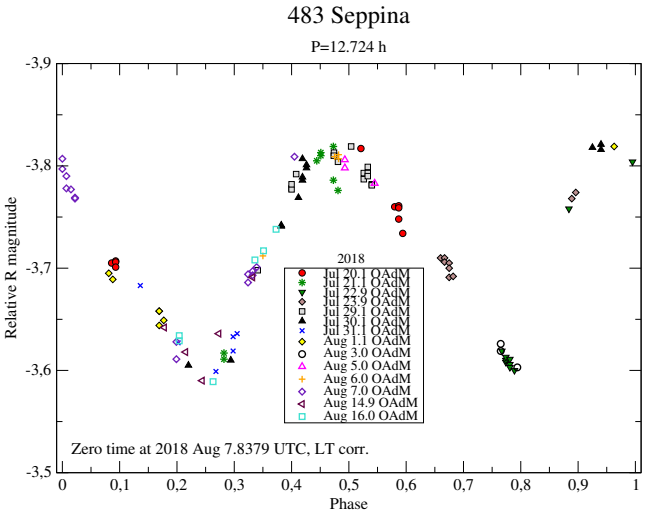

Fig. 71: Composite lightcurve of (483) Seppina from the year 2018.

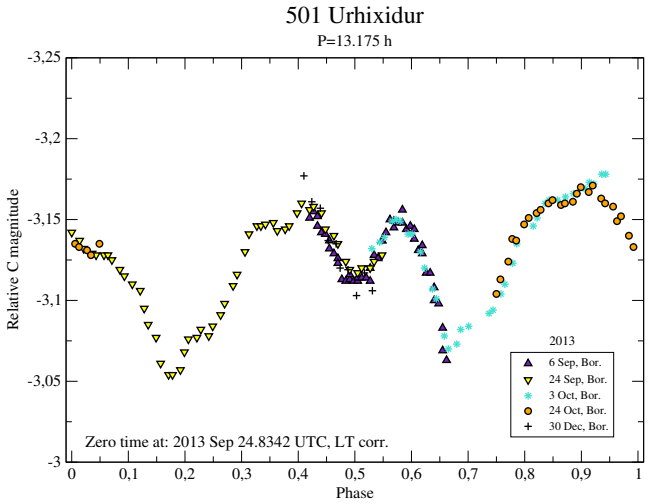

Fig. 72: Composite lightcurve of (501) Urhixidur from the year 2013.

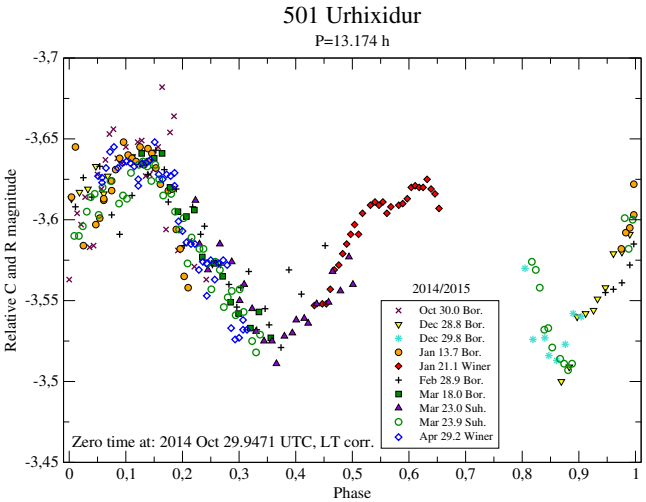

Fig. 73: Composite lightcurve of (501) Urhixidur from the years 2014-2015.

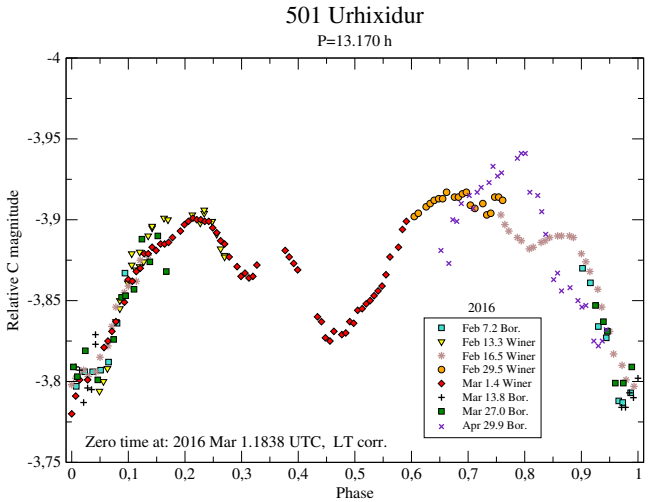

Fig. 74: Composite lightcurve of (501) Urhixidur from the year 2016.

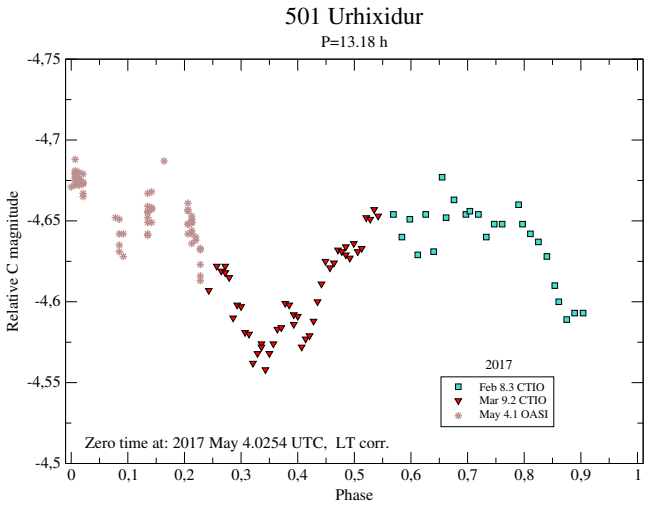

Fig. 75: Composite lightcurve of (501) Urhixidur from the year 2017.

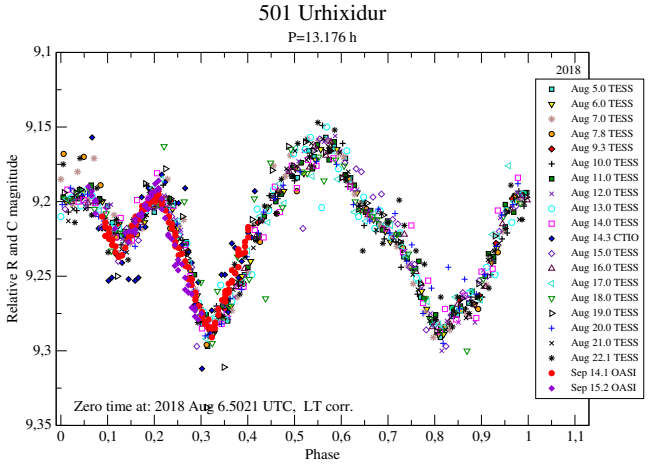

Fig. 76: Composite lightcurve of (501) Urhixidur from the year 2018.

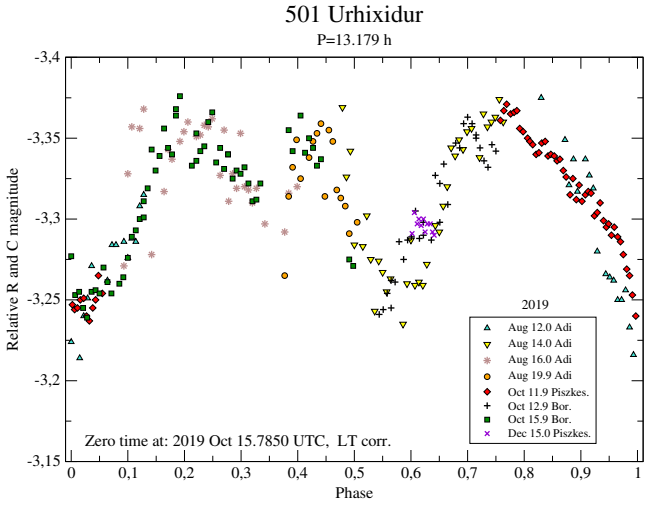

Fig. 77: Composite lightcurve of (501) Urhixidur from the year 2019.

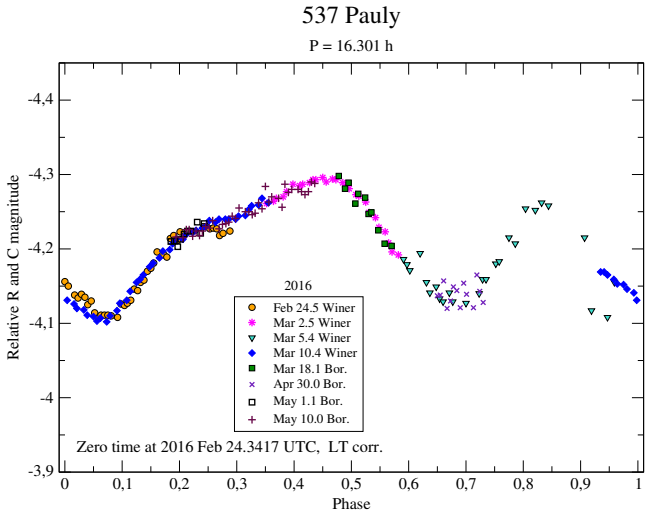

Fig. 78: Composite lightcurve of (537) Pauly from the year 2016.

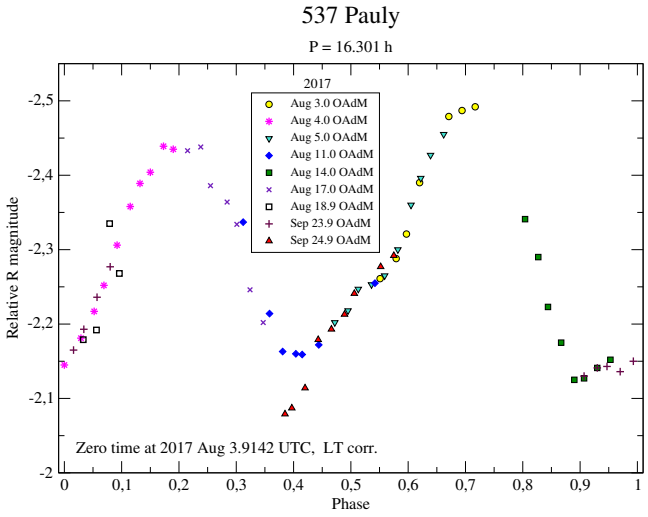

Fig. 79: Composite lightcurve of (537) Pauly from the years 2017.

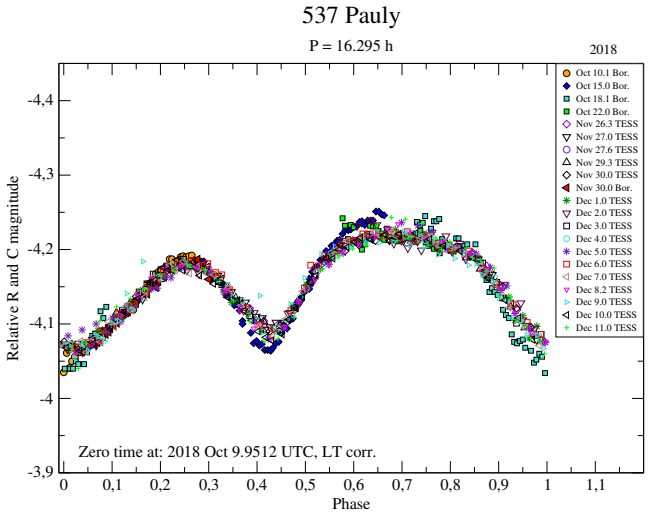

Fig. 80: Composite lightcurve of (537) Pauly from the year 2018.

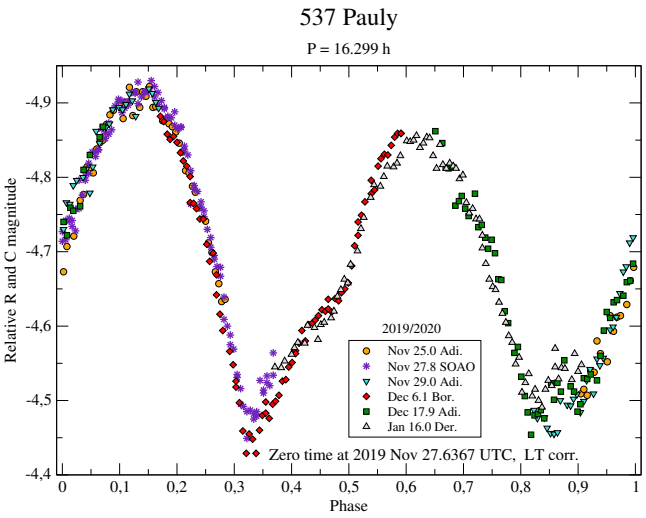

Fig. 81: Composite lightcurve of (537) Pauly from the years 2019-2020.

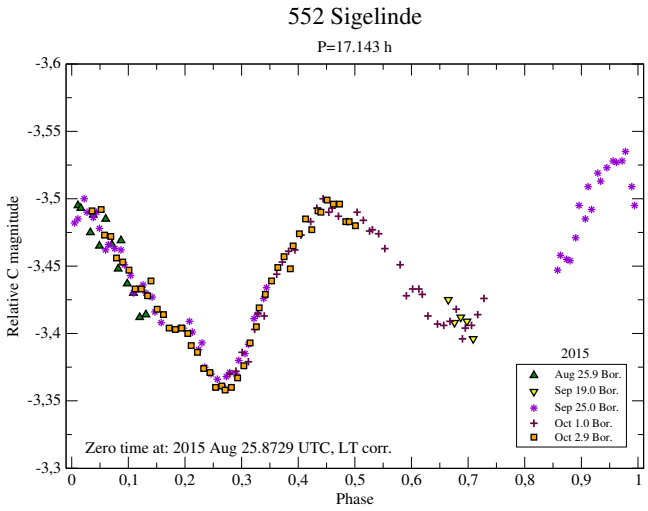

Fig. 82: Composite lightcurve of (552) Sigelinde from the year 2015.

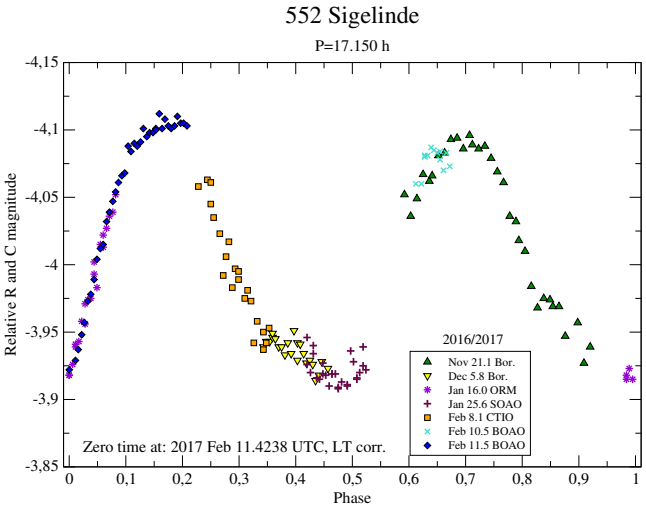

Fig. 83: Composite lightcurve of (552) Sigelinde from the years 2016-2017.

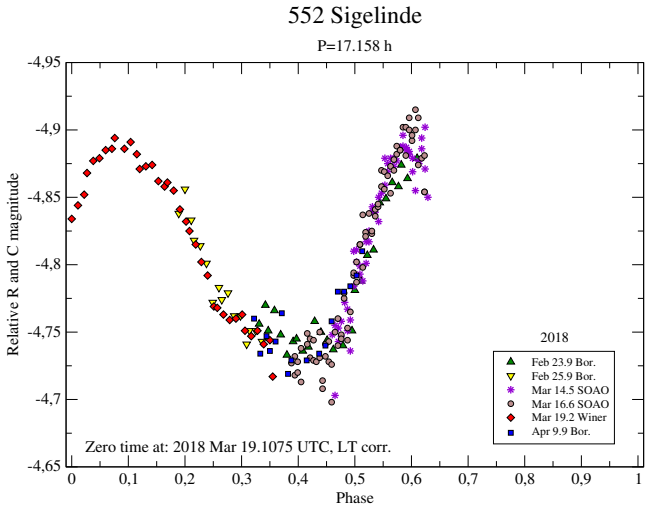

Fig. 84: Composite lightcurve of (552) Sigelinde from the year 2018.

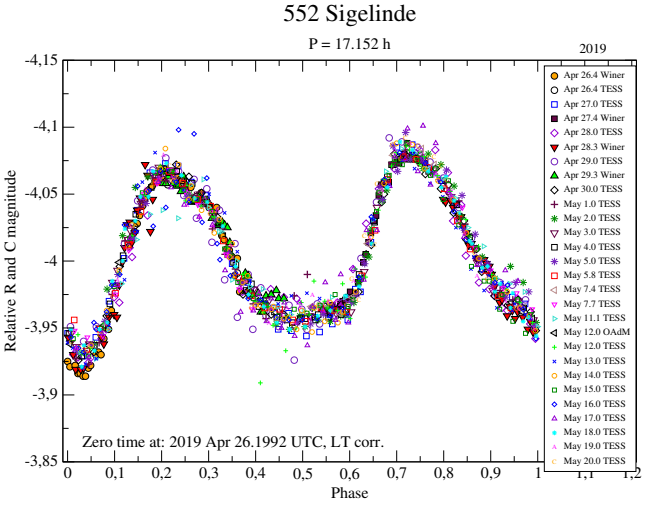

Fig. 85: Composite lightcurve of (552) Sigelinde from the year 2019.

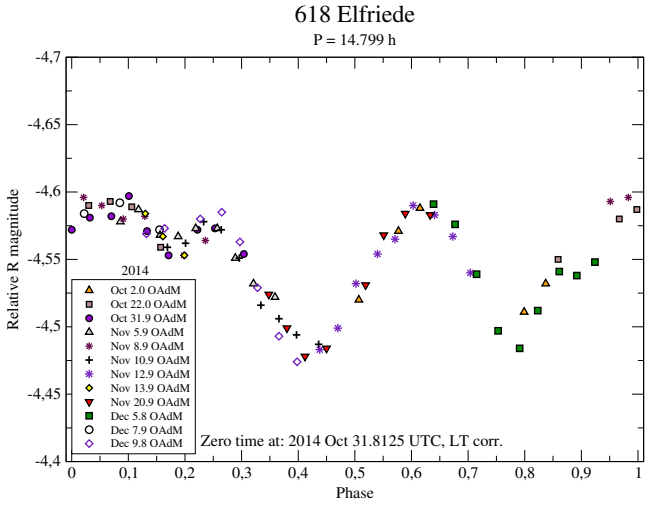

Fig. 86: Composite lightcurve of (618) Elfriede from the year 2014.

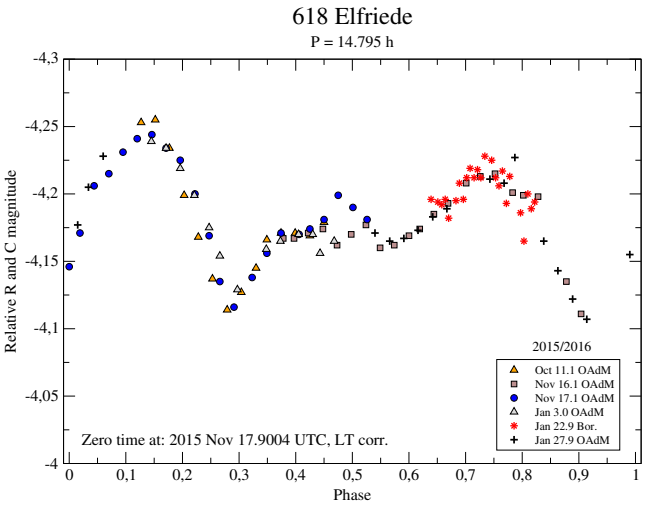

Fig. 87: Composite lightcurve of (618) Elfriede from the years 2015-2016.

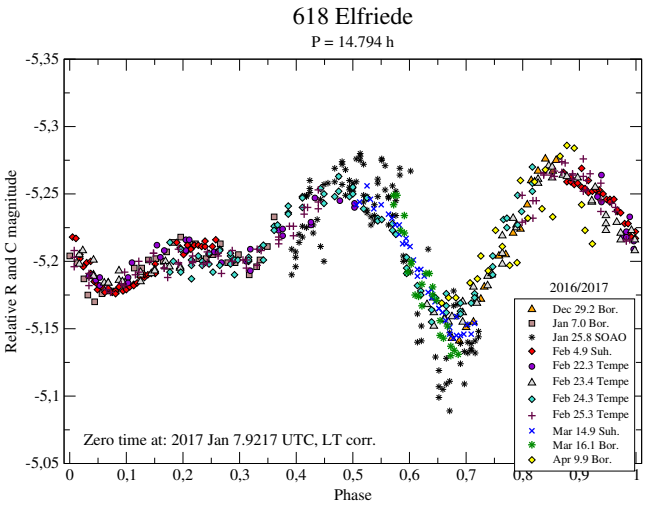

Fig. 88: Composite lightcurve of (618) Elfriede from the year 2017.

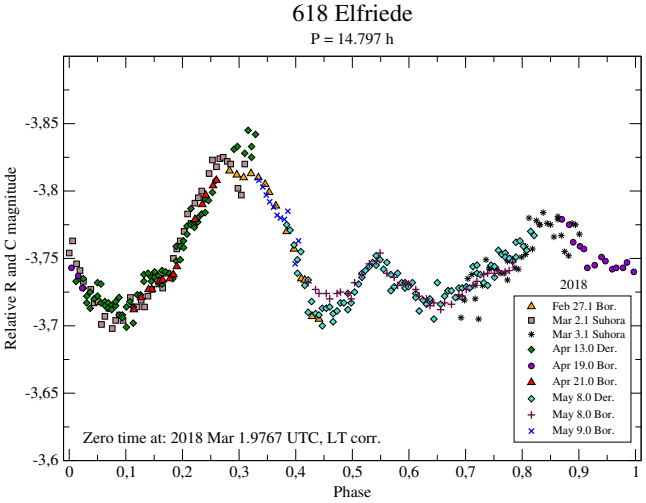

Fig. 89: Composite lightcurve of (618) Elfriede from the year 2018.

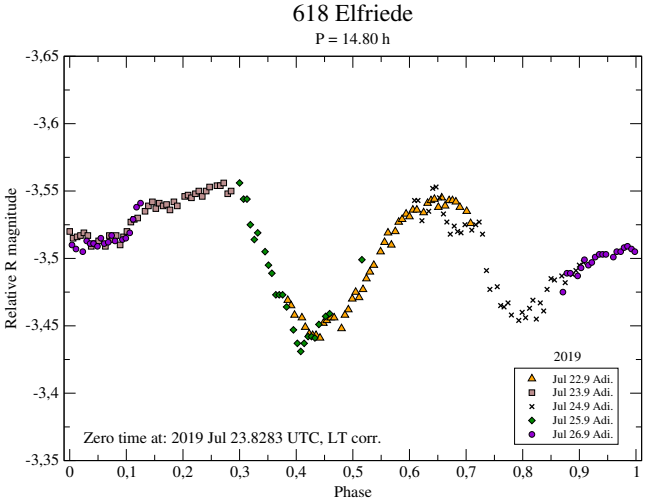

Fig. 90: Composite lightcurve of (618) Elfriede from the year 2019.

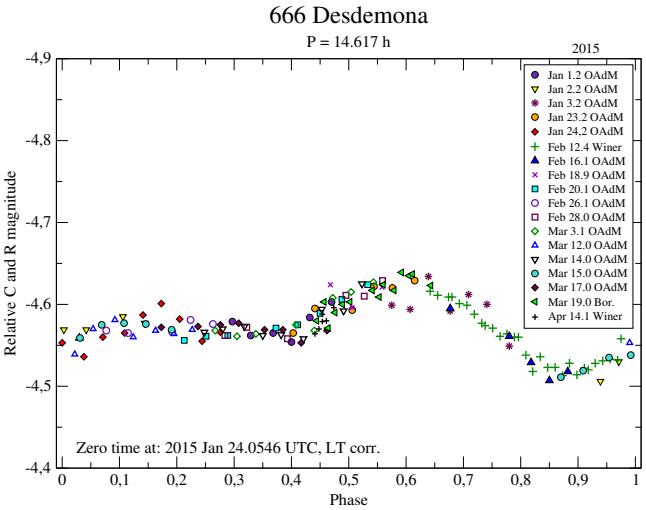

Fig. 91: Composite lightcurve of (666) Desdemona from the year 2015.

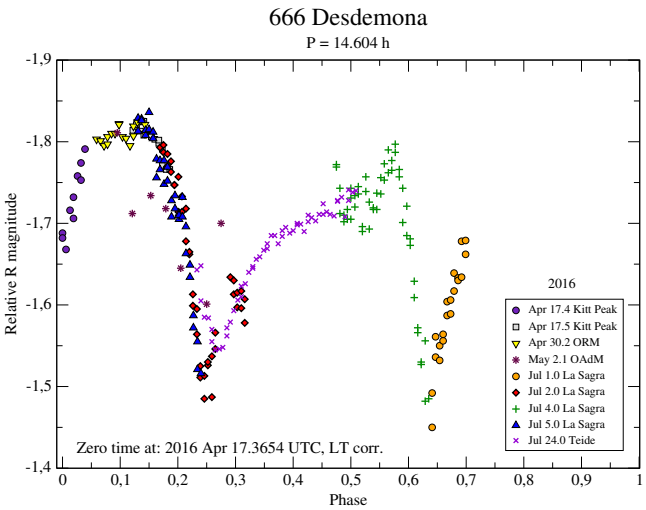

Fig. 92: Composite lightcurve of (666) Desdemona from the year 2016.

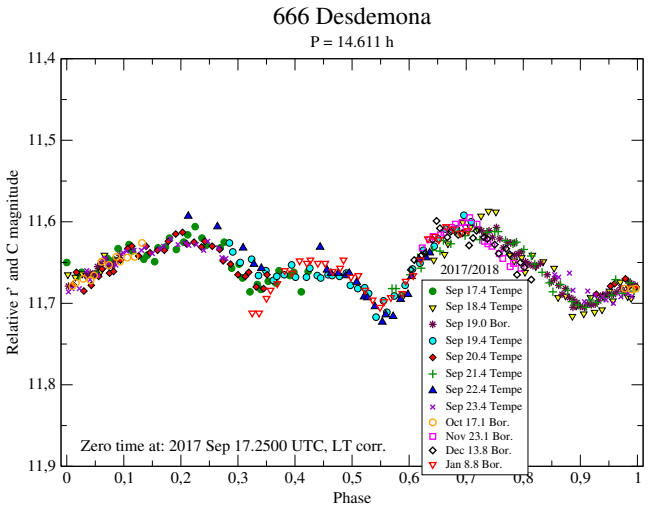

Fig. 93: Composite lightcurve of (666) Desdemona from the years 2017-2018.

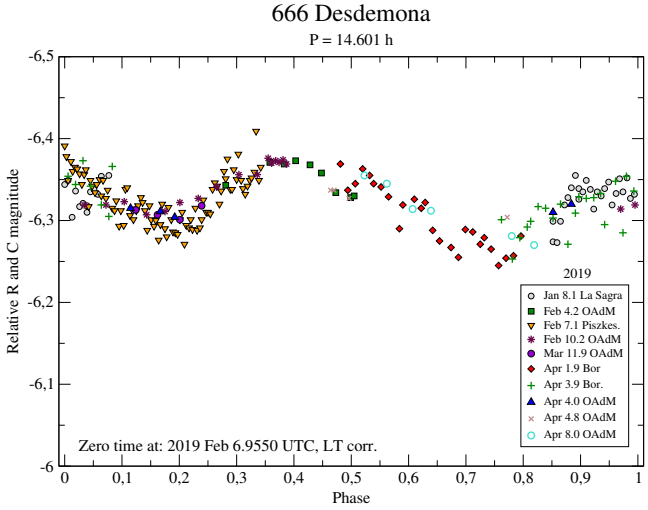

Fig. 94: Composite lightcurve of (666) Desdemona from the year 2019.

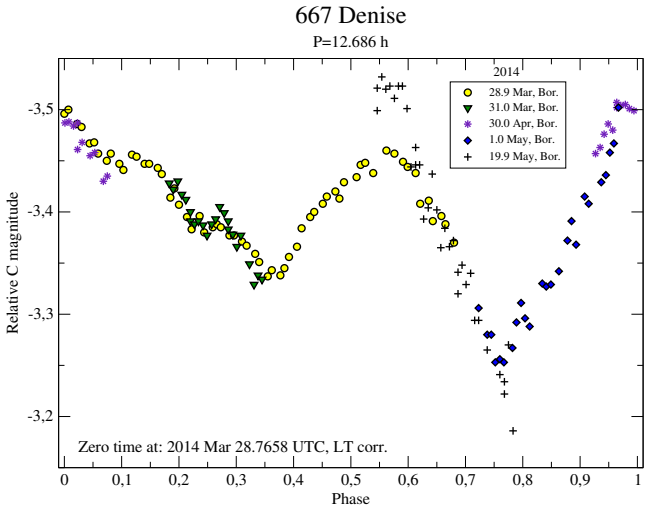

Fig. 95: Composite lightcurve of (667) Denise from the year 2014.

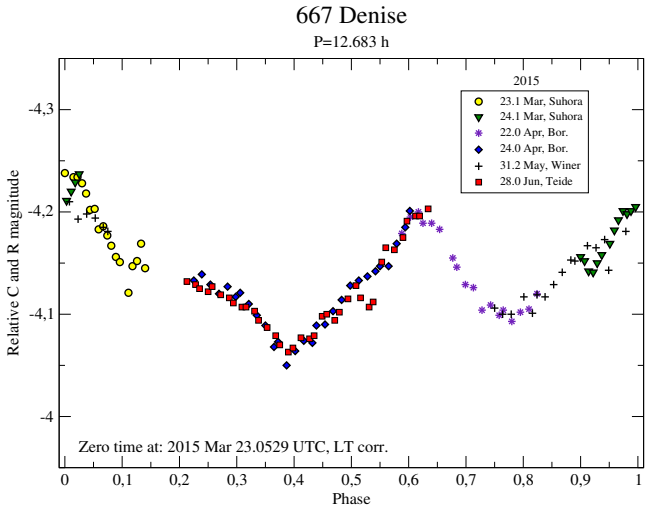

Fig. 96: Composite lightcurve of (667) Denise from the year 2015.

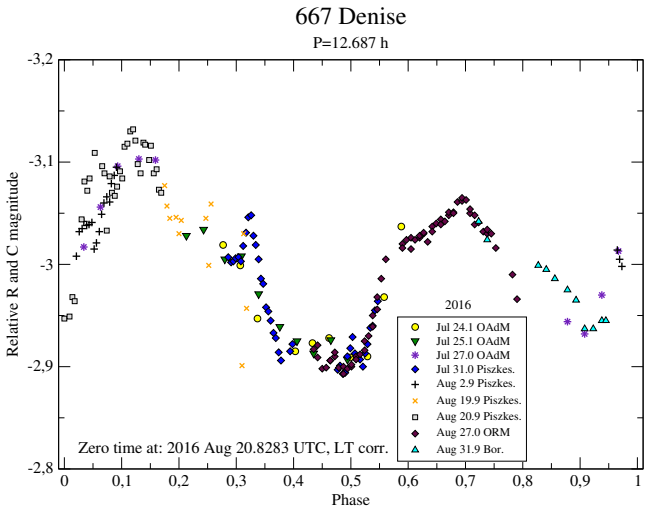

Fig. 97: Composite lightcurve of (667) Denise from the year 2016.

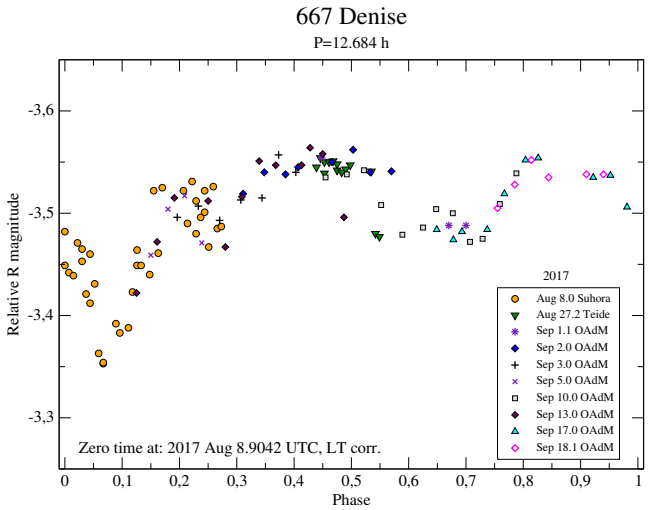

Fig. 98: Composite lightcurve of (667) Denise from the year 2017.

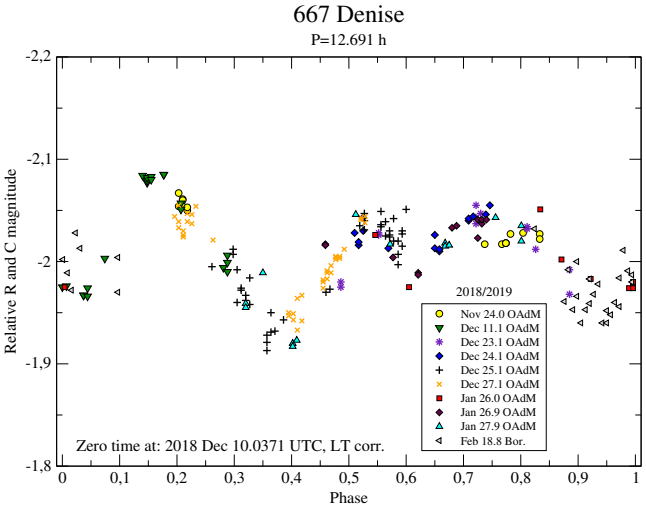

Fig. 99: Composite lightcurve of (667) Denise from the years 2018-2019.

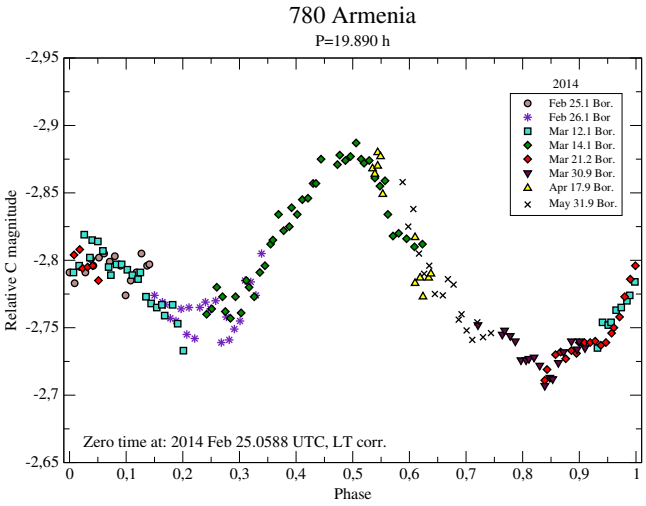

Fig. 100: Composite lightcurve of (780) Armenia from the year 2014.

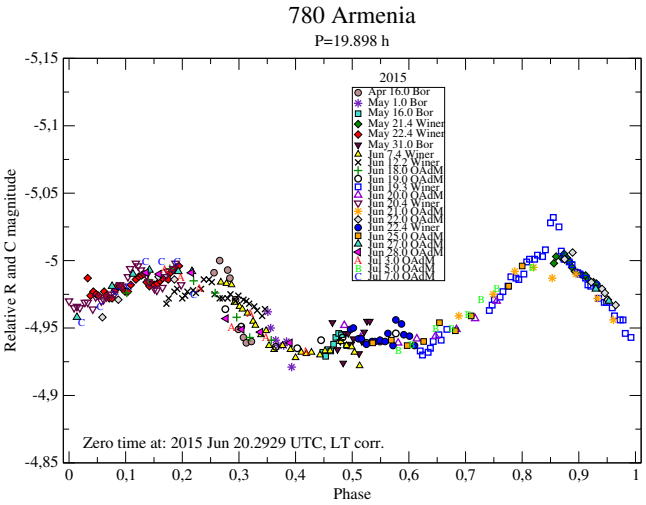

Fig. 101: Composite lightcurve of (780) Armenia from the year 2015.

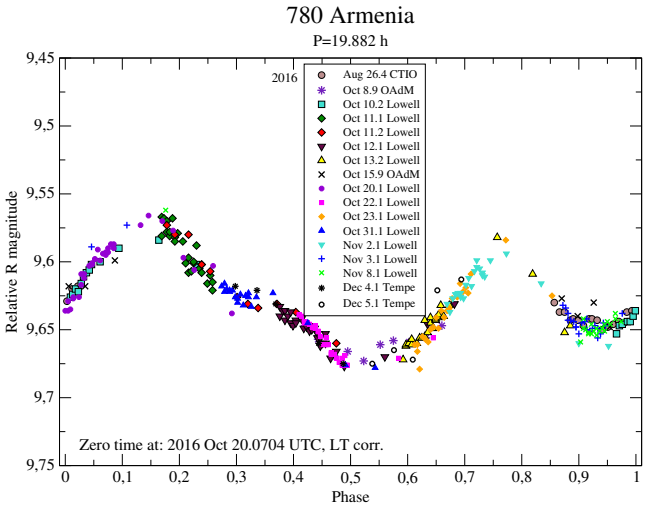

Fig. 102: Composite lightcurve of (780) Armenia from the year 2016.

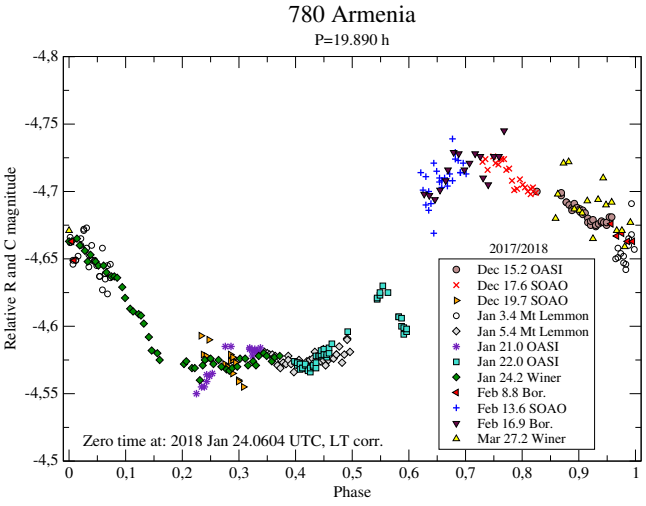

Fig. 103: Composite lightcurve of (780) Armenia from the years 2017-2018.

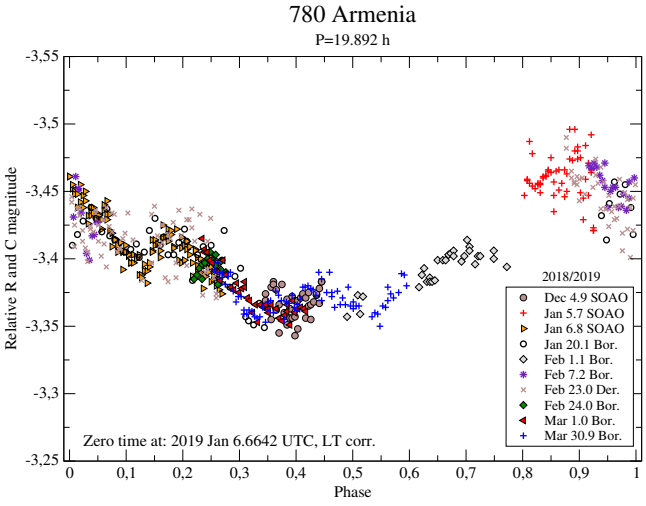

Fig. 104: Composite lightcurve of (780) Armenia from the years 2018-2019.

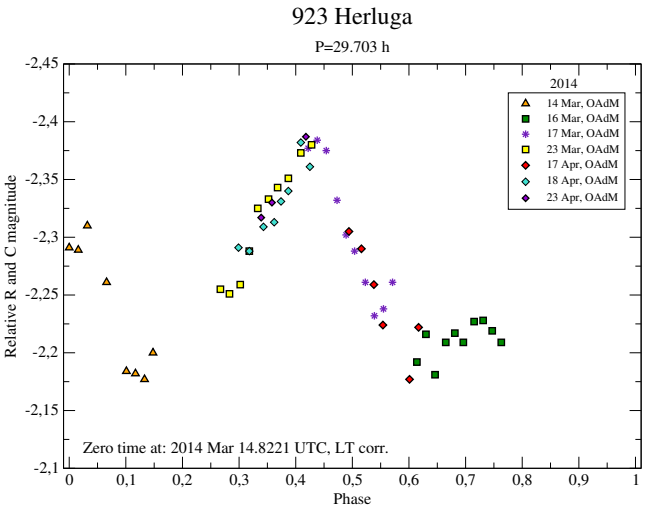

Fig. 105: Composite lightcurve of (923) Herluga from the year 2014.

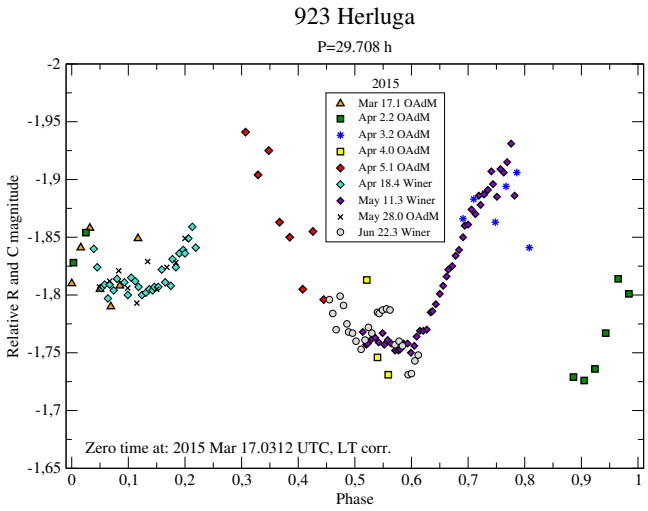

Fig. 106: Composite lightcurve of (923) Herluga from the year 2015.

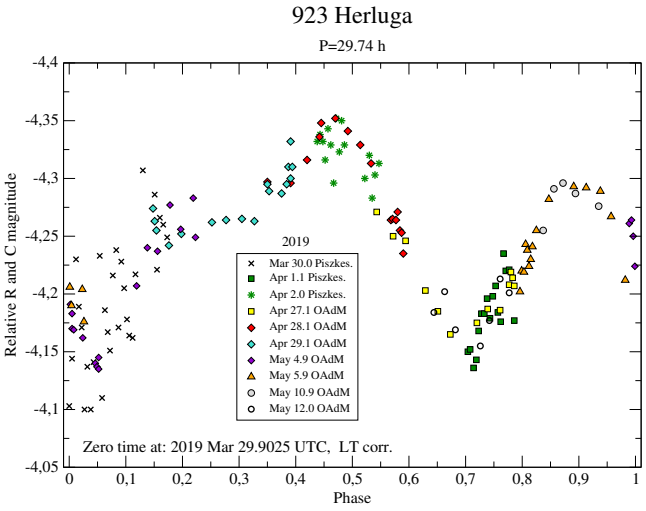

Fig. 107: Composite lightcurve of (923) Herluga from the year 2019.

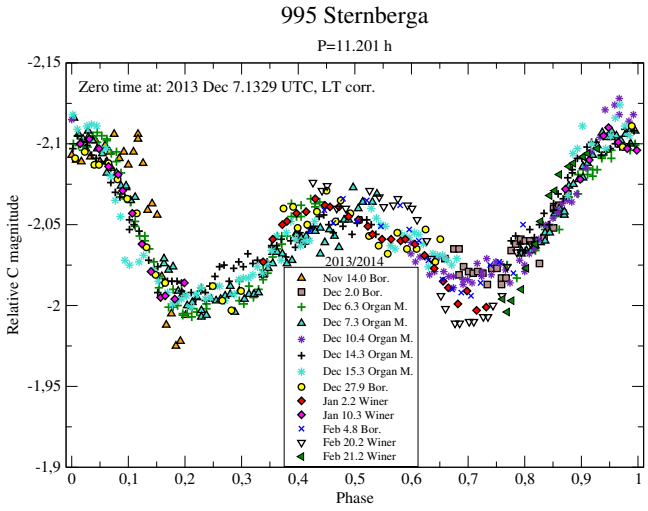

Fig. 108: Composite lightcurve of (995) Sternberga from the years 2013-2014.

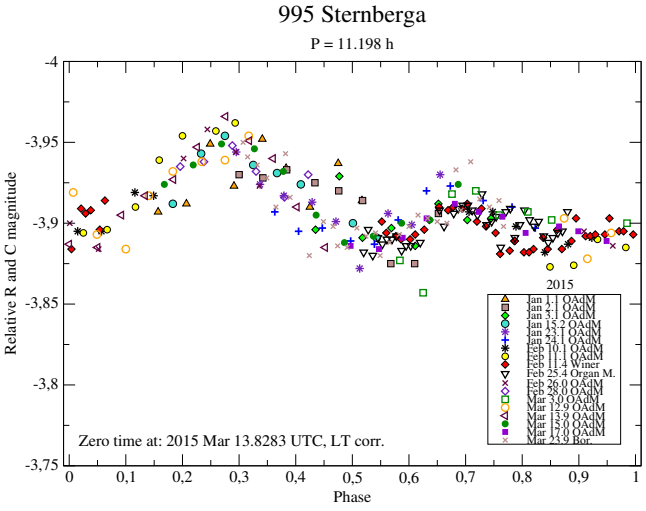

Fig. 109: Composite lightcurve of (995) Sternberga from the year 2015.

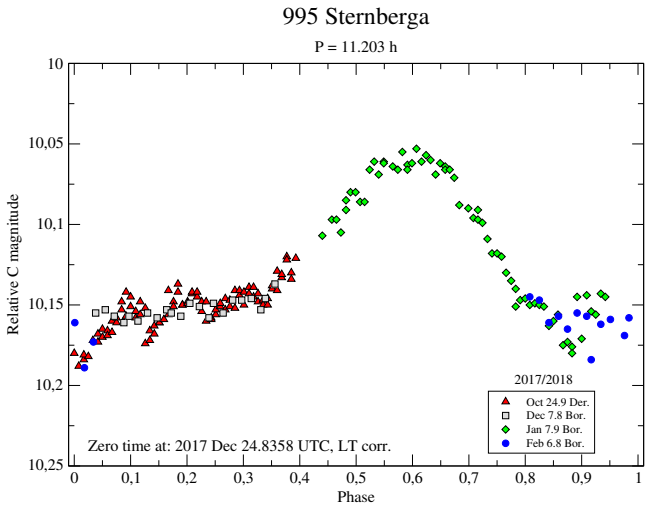

Fig. 110: Composite lightcurve of (995) Sternberga from the years 2017-2018.